Article:
Ma, CY and Roberts, KJ (2019) Morphological population balance modelling of the effect of crystallisation environment on the evolution of crystal size and shape of para-aminobenzoic acid. Computers & Chemical Engineering, 126. pp. 356-370. ISSN: 0098-1354

https://doi.org/10.1016/j.compchemeng.2019.04.019

Morphological Population Balance Modelling of the Effect of Crystallisation Environment on the Evolution of Crystal Size and Shape of Para-aminobenzoic Acid

C. Y. Ma and K. J. Roberts

Centre for the Digital Design of Drug Products, School of Chemical and Process Engineering, University of Leeds, Leeds, LS2 9JT, United Kingdom

Corresponding author:
Dr Cai Yun Ma
School of Chemical and Process Engineering
University of Leeds
Leeds LS2 9JT
UK
Tel +44 113 343 7809
Email c.y.ma@leeds.ac.uk

Abstract

A current morphological population balance (MPB) modelling methodology, which integrates crystal morphology, facet growth kinetics with multi-dimensional population balance, is overviewed and demonstrated, hence providing an attractive approach for modelling crystallisation processes. MPB modelling is applied to simulate the batch crystallisation of the alpha-form of para-aminobenzoic acid from ethanolic solutions as a function of the crystallisation environment including cooling rate, seeding temperature and seed conditions (loading, size and shape). The evolution of crystal shape/size and their distributions revealed that higher loading led to smaller and less needle-like crystals with similar yields, hence potentially being an important parameter for process control. Examination of the development of the fracture surface for broken seeds, mimicking the seed conditions after milling in practice in the simulated processes, demonstrated that these faces grew fast and then rapidly disappeared from the external crystal morphology. Restriction and challenges inherent in the current model are also highlighted.

Keywords: Morphological Population Balance, Crystal Shape Distribution, Crystal Size Distribution, Crystallisation, Para-aminobenzoic Acid, Crystallisation Environment

1. Introduction

Recent reviews (Bell, 2017, Maier, 2017) have highlighted that the development of new technologies has the potential to deliver a step-change in the way we make medicines through the adoption of state-of-the-art simulation-based tools. Through this, more 'near patient' medicines (combination medicines, wider range of dosage forms, stratified formulation) can be delivered through the much greater agility provided by digital design and automation. Digital design potentially provides the route to the preparation of the solution re-crystallised pharmaceuticals which have e.g. low structural variability, high purity and narrow size/shape distribution with concomitantly enhanced product properties. Such materials could have significant patient benefits such as narrow therapeutic profiles, higher stability and longer shelf life, greater content uniformity, etc. and as such represent a critical objective for the delivery of medicines with pre-defined properties for industry and society. Active pharmaceutical ingredient (API) and excipients used in their formulation often have well-defined crystal morphologies and hence surface chemistry, and thus their physical properties can be defined and manipulated through modelling, optimisation and control of crystallisation processes. Such surface properties can provide the key parameters for delivering both drug product quality (such as high purity and lack of variability) and performance (such as bioavailability and stability), and also ensuring the same particles encompassed within the API are present in the formulated drug product and are also transferred from R&D into manufacturing stage.

Most drugs are still manufactured in the traditional way, i.e. through processes designed to deliver tasks such as crystallisation for enabling product purity, form and yield. However, each of these discrete steps is not necessarily considering and/or directly linking with their resultant effect of the resultant crystal properties on the downstream processes. Therefore, a crystallisation process generally produces crystals with dispersion of size/shape. However, for the growing area of targeted medicines, such variations create challenges as they have mindful of their potentials to affect the drug crystal's dissolution and hence its efficacy, i.e. crystals with different sizes/shapes create variability in the in-vitro dissolution. Currently, to achieve the required size/shape and their distributions for drug formulation, crystal particles are milled to effect the size reduction needed. However, such intensive mechanical processing can impact on the crystal's surface properties through the creation of new high surface energy, fracture surfaces and lattice defects such as dislocations, as well as significantly enhancing surface roughness and hence area. In extreme cases, milling can cause polymorphic form transformation. Similarly, blending/granulation for mixing with binder/excipients to produce granules may need to be broken into smaller size for compaction/tableting processes. In principle, crystals and excipients could be produced with a much tighter specification such that they could be directly compressed and tabletted into the final product without the need for milling and

granulation processes, and also avoiding variability due to changes in, and/or damage to, crystal surface properties. In pharmaceutical product development, crystallisation processes are widely used but many ingredients exhibit needle-like, plate-like or rod-like crystal morphologies, which can directly affect their downstream particle processing properties such as filterability, flowability, tabletability. Therefore, digital design of crystallisation processes based on first-principles physical chemical models can become an important bottleneck to breakthrough.

Traditional population balance (PB) models use a length (or radius of a volume equivalent sphere) for one-dimensional characteristic size or length and width for two-dimensional characteristic sizes with a shape factor for calculating crystal volume. Assuming the crystal morphology does not change during crystallisation processes, the evolution of crystal shape/size could be represented (e.g., (Lovette et al., 2008, Zhang and Doherty, 2004, Kuvadia and Doherty, 2013)). Morphological PB (MPB) (e.g. (Ma et al., 2008)) was developed to remove the assumption that crystal morphology is invariant during crystallisation, through directly integrating both base crystal morphology and face-specific growth kinetics with the PB model, hence capturing the change of crystal shape/size and through this their face $\{hkl\}$-specific properties. A more detailed review of previous work is given in Supplementary materials (S1).

In this paper, the MPB method is overviewed and demonstrated through a numerical study of a pharmaceutical compound, α-*p*ABA, crystallised from ethanolic solution. In this, the face-specific growth mechanisms and rate equations were obtained by fitting the experimental data as obtained from the literature (Toroz et al., 2015). The performance of crystallisation processes is examined using MPB modelling to predict the evolution of crystal shape/size distributions in a seeded batch cooling crystalliser under different cooling rate, seeding and seed conditions including assessing the impact of broken seeds on the properties of the final products.

2. Morphological Population Balance for Crystallisation Process Design

2.1 MPB Modelling Framework

The framework for prediction of the distributions of crystals size and shape for crystallisation processes using MPB modelling is schematically shown in Figure 1. For the known crystal shape and size, the centre of the crystal and the corresponding normal distances from individual faces, which can be defined by the Miller Index $\{hkl\}$ (a notion system in crystallography for crystal planes/faces) such as $\{h_1k_1l_1\}$, $\{h_2k_2l_2\}$ and $\{h_3k_3l_3\}$ in Figure 1, to the centre can be determined with individual variables such as x_1, x_2 and x_3 in Figure 1. During crystallisation processes, these variables are under continuous evolution as the processes are controlled by various crystallisation mechanisms including

nucleation, growth, agglomeration, breakage and crystallisation environment. Therefore these variables can be treated as the independent variables for the formulation of MPB equation. As shown in Figure 1, nucleation, face-specific growth kinetics, face-based agglomeration and breakage kernels are the key input parameters for MPB modelling, which can be determined through various modelling and experimental studies. The solution of the MPB equation will generate the evolution of these independent variables, i.e. normal distances, of all crystals, hence their distributions at each crystallisation time. Based on the known crystal morphology, each combination of normal distances (x_1, x_2, x_3) represents a crystal shape with the distribution providing the number of crystals having this shape. Therefore, after the crystal size/shape analysis, a crystal shape distribution can be formed and examined to see whether the distribution meets the requirements for precision particles. If not (Figure 1), the MPB can optimise and control the crystallisation environment, hence achieving the required crystal shape distribution.

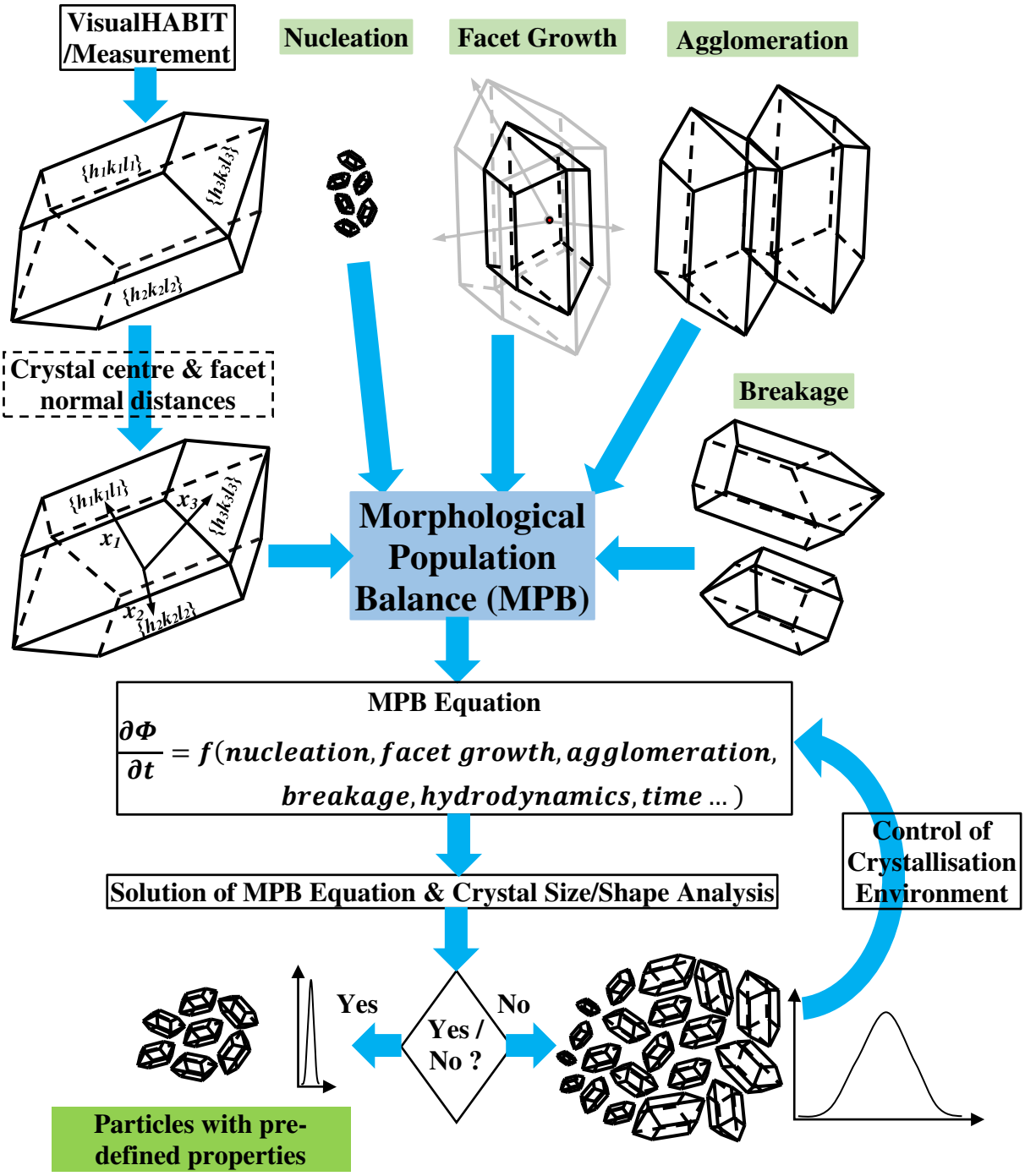

Figure 1. Schematic of a framework for digital design of crystals with pre-defined size/shape and their distributions using MPB modelling. Note that $\{h_1k_1l_1\}$, $\{h_2k_2l_2\}$ and $\{h_3k_3l_3\}$ are the Miller Indices of the crystal and x_1, x_2 and x_3 are the corresponding normal distances from the individual faces to the centre of the crystal, Φ and t are the number population density function of crystals and crystallisation processing time, respectively.

2.2 MPB Model Formulation

The general PB model formulation to describe particulate systems with internal and external variables can be found in literature (e.g., (Hulburt and Katz, 1964, Ramkrishna and Mahoney, 2002, Randolph and Larson, 1988)). In this study, the MPB methodology identifies and defines the normal distances from faces ($\{h_1k_1l_1\}$, $\{h_2k_2l_2\}$ and $\{h_3k_3l_3\}$) to the crystal centre as three independent dimension variables (x_1, x_2, x_3), respectively, as shown in Figure 1. The PB equation for seeded batch cooling crystallisation processes in a well-mixed batch crystalliser without nucleation, agglomeration and breakage to simplify the case study of MPB for pharmaceutical crystallisation can be written as (e.g., (Ma and Roberts, 2018, Ma et al., 2008, Marchal et al., 1988, Puel et al., 2003)):

$$\frac{1}{V_T(t)}\frac{\partial}{\partial t}[\Phi(x_1,x_2,x_3,t)V_T(t)] + \frac{\partial}{\partial x_1}[\Phi(x_1,x_2,x_3,t)G_1(x_1,t)] + \frac{\partial}{\partial x_2}[\Phi(x_1,x_2,x_3,t)G_2(x_2,t)] + \frac{\partial}{\partial x_3}[\Phi(x_1,x_2,x_3,t)G_3(x_3,t)] = 0 \quad (1)$$

where V_T is the total volume of solution (or slurry after seeding) in a crystalliser; t is the processing time; Φ is the number population density function of crystals; G_i (i = 1, 3) is the growth rate in the x_i (i = 1, 3) direction. The corresponding initial condition is the size/shape distribution as a function of the three variables (x_1, x_2, x_3) at the time of zero, i.e., $\Phi(x_1,x_2,x_3,t)|_{t=0} = 0$. For a batch cooling crystallisation process, the boundary conditions for Eq. (1) are $\Phi(x_{1,i},x_{2,j},x_{3,k},t)|_{i=1 \text{ or } N_1} = 0$ (j = 1, N_2; k = 1, N_3), $\Phi(x_{1,i},x_{2,j},x_{3,k},t)|_{j=1 \text{ or } N_2} = 0$ (i = 1, N_1; k = 1, N_3) and $\Phi(x_{1,i},x_{2,j},x_{3,k},t)|_{k=1 \text{ or } N_3} = 0$ (i = 1, N_1; j = 1, N_2), where N_1, N_2, N_3 are the total number of classes for the (x_1, x_2, x_3) size domains (see the Supplementary materials (S3) for the definitions of other parameters). It is worth to note that three dimensions (x_1, x_2, x_3) are not Cartesian coordinates, hence they are not perpendicular to each other. Furthermore, depending on the number of independent crystal faces identified, the MPB techniques can generate the MPB equation with the corresponding number of dimensions. The growth rates of individual faces such as ($\{h_1k_1l_1\}$, $\{h_2k_2l_2\}$ and $\{h_3k_3l_3\}$) can be obtained through fitting with measured crystal growth data (see more detail in the Supplementary materials (S2)). The discretisation method can be used to form multi-dimensional ordinary differential equations for their solution with a standard solver such as the Runge-Kutta-Fehlbergh solver (see further details in the Supplementary materials (S3) and Section 3.2).

3. MPB Modelling of α-*p*ABA Crystallised from Ethanolic Solutions

3.1 Materials and Solute-Solvent System

The organic compound, para aminobenzoic acid, provides an important representative compound for fundamental study (Rosbottom et al., 2017, Rosbottom, 2016, Toroz et al., 2015, Rosbottom et al., 2015, Sullivan et al., 2014, Nguyen et al., 2014). The α polymorphic form, α-*p*ABA, can be readily crystallised from ethanol solvent in a 0.5L batch crystalliser using a seeded cooling process. The *p*ABA molecular structure shows that it consists of a phenyl ring with a carboxylic acid group and an amino group in the para position (Rosbottom et al., 2015). Through crystallographic studies and molecular modelling, the α-*p*ABA crystal morphology (Figure 2) can be characterised by 8 stable crystal faces (2 {101}, 2 {10-1} and 4 {011} faces) in a monoclinic crystal structure with the space group $P2_1/n$ (Rosbottom et al., 2015). The α-*p*ABA crystal structure comprises two molecules in the asymmetric unit and eight molecules in the unit cell with cell dimensions: a = 18.55 Å, b = 3.86 Å, c = 18.64 Å and β = 93.56° (a, b, c and β are the unit cell parameters) The intermolecular packing arrangement within the structure is dominated by the formation of two non-equivalent OH···O H-bonding dimers between neighbouring carboxylic acid groups, and also by π - π stacking interactions created by the head to heat stacking motif of the *p*ABA molecules along the b direction. Overall, the α form of *p*ABA crystal is observed to have a needle-like or lath-like morphology elongated along the b-crystallographic axis which is a typical crystal shape for many pharmaceutical solids. Further detail can be found in literature (Rosbottom et al., 2015, Toroz et al., 2015).

Based on the crystal morphology of α-*p*ABA (Figure 2) and the definition of independent variables for MPB modelling in Section 2, the three variables for MPB simulation of α-*p*ABA crystallisation from ethanol can be determined as shown in Figure 2.

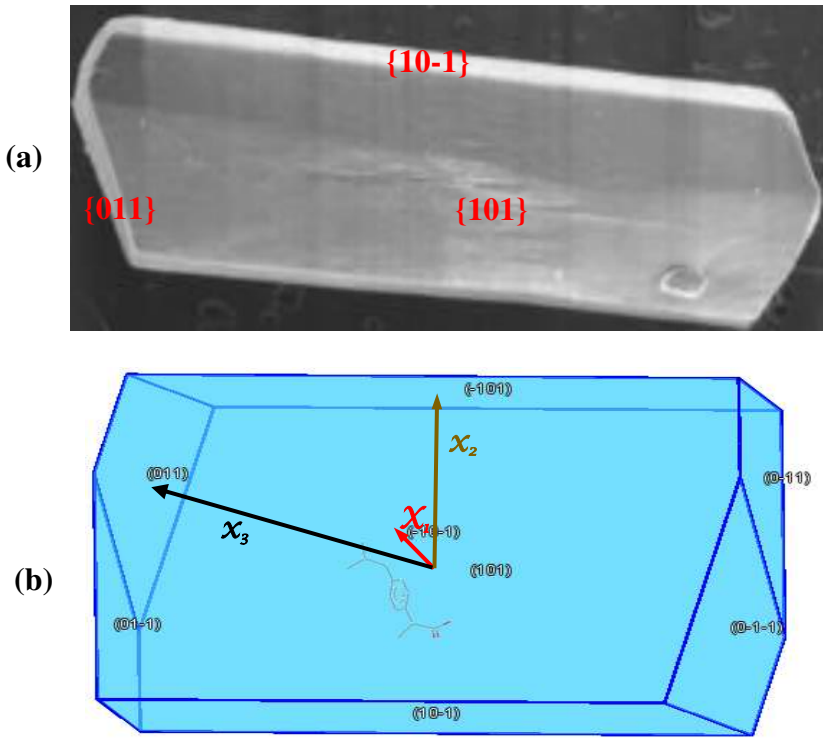

Figure 2. The α-*p*ABA crystal shape (single crystal image from (Rosbottom, 2016) and prediction by VisualHABIT (Clydesdale et al., 1991, Clydesdale et al., 1996, Pickering et al., 2017)) and the definitions of the three independent dimension variables (x_1, x_2, x_3) perpendicular to its three dominant crystal faces {101}, {10-1}, {011} for MPB modelling.

The solubility of α-*p*ABA in ethanol solvent were obtained from literature (Toroz et al., 2015, Rosbottom et al., 2017) using an isothermal technique. The experiments were carried out at the 1.5 ml scale with 300 rpm micro magnetic-bar stirring using an Avantium Crystal16 unit.

The facet crystal growth rates in the x_1, x_2 and x_3 face directions of α-*p*ABA growing in ethanol were measured by an optical microscopy in a crystal growth cell (Toroz et al., 2015), with more detail to be found in (Toroz et al., 2015, Nguyen et al., 2014).

3.2 Crystallisation Environment and MPB Solution

The obtained three dimensional MPB equation, together with available solubility and faceted growth rate equations based on single crystal experimental data from Toroz et al. (Toroz et al., 2015), was solved with the following operating conditions: cooling rate (*CR*) of 0.5°C/min, saturation concentration of 0.222 kg/kg (saturated temperature of 45°C), seeding point of 20.5°C with the corresponding supersaturation, *S*, (= solute concentration (*C*) / solubility) of 1.5, seed loading of 0.1% (by mass), and seed mean x_1, x_2 and x_3 of 22, 37 and 58 μm. Using the above operating conditions as

263 a base case (green coloured in Table 1), further simulations were carried out to investigate the effect
264 of different operating conditions (Table 1) on the crystal size/shape evolution of α-*p*ABA
265 crystallisation, including different *CR* of 0.05 – 1.5°C/min, various seeding temperatures (T_{seeds}) of
266 20.5 – 39.0°C (corresponding to supersaturation at the seeding points (S_{seeds}) of 1.5 – 1.1), different
267 seed loadings (X_{seeds}) of 0.1 – 5.0%, initial mean size/shape of seeds (M_{seeds} ($\bar{x}_1, \bar{x}_2, \bar{x}_3$) are the mean
268 sizes of variable (x_1, x_2, x_3) and the corresponding ($\sigma_{x_1}, \sigma_{x_2}, \sigma_{x_3}$) are the standard deviations), and
269 other special operating conditions such as broken seeds. All of the simulations were terminated when
270 the supersaturation reached to 1.01, indicating that crystal growth in all face directions became close
271 to zero, hence any further crystallisation process would not vary the size/shape distributions, yield of
272 the final products.

273

274 **Table 1.** Operating conditions used for MPB simulations

Cooling rate (*CR*)							
CR (°C/min)	Saturation concentration *C* (kg/kg)	Saturation *T* (°C)	Seeding point – T_{seeds} (°C)	S_{seeds} (-)	X_{seeds} (% mass)	M_{seeds} ($\bar{x}_1, \bar{x}_2, \bar{x}_3$) (μm)	Seeds standard deviations - ($\sigma_{x_1}, \sigma_{x_2}, \sigma_{x_3}$) (μm)
0.05	0.222	45	20.5	1.5	0.1	22, 37, 58	8, 8, 8
0.5	0.222	45	20.5	1.5	0.1	22, 37, 58	8, 8, 8
1.0	0.222	45	20.5	1.5	0.1	22, 37, 58	8, 8, 8
1.5	0.222	45	20.5	1.5	0.1	22, 37, 58	8, 8, 8
Seeding point (T_{seeds} or S_{seeds})							
0.5	0. 222	45	39.0	1.1	0.1	22, 37, 58	8, 8, 8
0.5	0. 222	45	33.7	1.2	0.1	22, 37, 58	8, 8, 8
0.5	0. 222	45	28.9	1.3	0.1	22, 37, 58	8, 8, 8
0.5	0. 222	45	24.7	1.4	0.1	22, 37, 58	8, 8, 8
0.5	0. 222	45	20.5	1.5	0.1	22, 37, 58	8, 8, 8
Seed loading (X_{seeds})							
0.5	0. 222	45	20.5	1.5	0.1	22, 37, 58	8, 8, 8
0.5	0. 222	45	20.5	1.5	0.5	22, 37, 58	8, 8, 8
0.5	0. 222	45	20.5	1.5	1.0	22, 37, 58	8, 8, 8
0.5	0. 222	45	20.5	1.5	2.0	22, 37, 58	8, 8, 8
0.5	0. 222	45	20.5	1.5	5.0	22, 37, 58	8, 8, 8
Seed mean shape (M_{seeds})							
0.5	0. 222	45	20.5	1.5	0.1	22, 37, 58	8, 8, 8
0.5	0. 222	45	20.5	1.5	0.1	22, 27, 40	8, 8, 8
0.5	0. 222	45	20.5	1.5	0.1	22, 27, 131	8, 8, 8

275

The typical seeds distributions for perfect and broken crystals are shown in Figure 3. With fixed mean sizes, M_{seeds}, $(\bar{x}_1, \bar{x}_2, \bar{x}_3)$ of (22, 37, 58µm) and standard deviations$(\sigma_{x_1}, \sigma_{x_2}, \sigma_{x_3})$ of (8, 8, 8µm), a Gaussian distribution of seeds crystals, $\Phi(x_1, x_2, x_3, 0)$, can be obtained using the pre-defined seeds loading (X_{seeds}). With the same amount of seed loading, the case with broken seeds (Figure 3b) has higher number of crystals. In Figure 3b, the bottom horizontal axis, z, is based on the face {011} at the side without breakage, i.e. the right side of the crystals, whilst the top horizontal axis is based on the broken face (010).

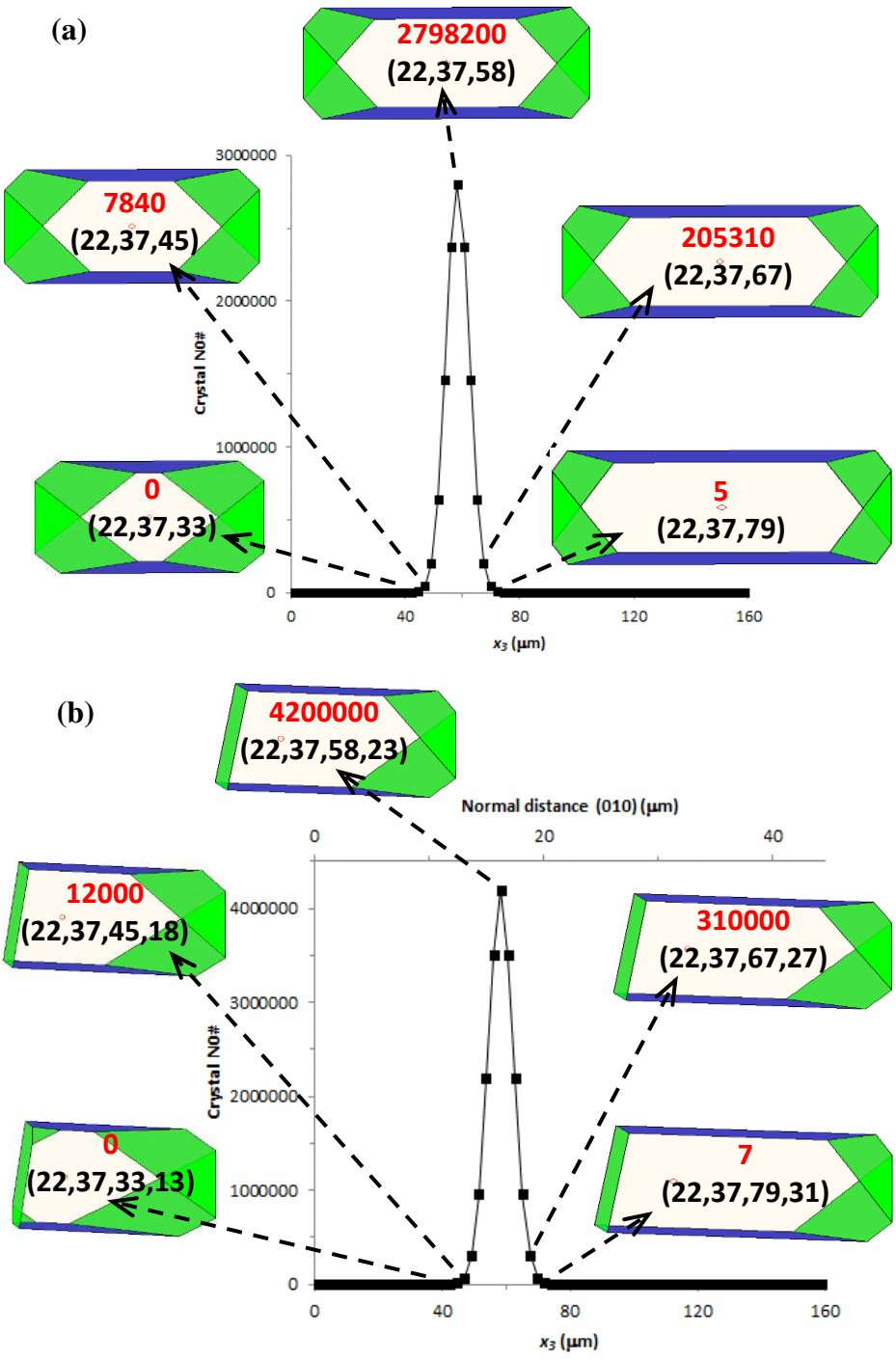

Figure 3. Typical seeds shape/size distributions: (a) perfect seed crystals, (b) broken seed crystals at the mean normal distances of faces {101} and {10-1}, i.e. x_1 and x_2. Note that the three values in the brackets in a) represent the normal distances of faces {101}, {10-1} and {011}, and the first three values in the brackets in b) represent the normal distances of faces {101}, {10-1} and {011} with the fourth one for the broken face (010).

With the MPB equation and discretisation method described in the Section 2.2 and Supplementary materials (S3), respectively, the (x_1, x_2, x_3) 3D domain of normal distances was discretised into (70, 70, 70) classes over the size ranges of three normal distances. The discretised MPB equations, together with a Gaussian-type initial distribution of seeds size/shape (as shown in Figure 3), and the other operating conditions (as listed in Table 1), were solved using the Runge-Kutta-Fehlbergh $4^{th}/5^{th}$-order solver (Shampine and Watts, 1977) with an automatic time-step control to obtain the evolution of normal distances in three face directions.

4. Results and Discussion

4.1 Solubility and Facet Growth Rates

The data obtained from literature (Toroz et al., 2015) were analysed to obtain the following solubility equation:

$$C^* = e^{\left(-\frac{1568}{T} + 2.3333\right)} \tag{2}$$

where T is the solution temperature (°C).

The experimental data of face-specific experimental data of growth rates of single crystals in a growth cell was collected by Toroz et al. (Toroz et al., 2015). The corresponding growth cell setup can be found in Nguyen et al. (Nguyen et al., 2014, Turner et al., 2019). Based on the experimental data (Toroz et al., 2015) and the face-specific growth kinetics described in the Supplementary materials (S2), the fit of growth rate in the face direction of {011} as a function of supersaturation was found to correspond to an RIG mechanism (r = 1 in Eq. (S.1)) even at low supersaturations. The corresponding facet growth rate of face {011}, G_3, is as follows:

$$G_3 = G\{011\} = \frac{S-1.0015}{8.65\times10^{-4}+\frac{1}{2.0\times10^{5}\times(S-1.0015)^{0}}} \tag{3}$$

From Eq. (3), it can be seen that the diffusion related term with a value of 8.65×10^{-4} is over 2 times magnitude larger than that for the surface integration term (5×10^{-6}). Therefore the rate of crystal

growth of face {011} is diffusion limited by diffusion mass transfer (Camacho et al., 2016), i.e. the crystal growth is controlled by how fast the solute molecules in bulk solution diffuses from the bulk solution and across the solid/solution boundary layer for integrating with (growing on) the crystal face. From molecular modelling studies (Rosbottom et al., 2015, Toroz et al., 2015), the π - π interactions dominate the growth on the {011} faces and the attachment of *p*ABA molecules via the π - π stacking motif may lead to a solid-solid integration mechanism at the surface, hence any growth spirals present at this surface. Therefore the diffusion of molecules to the surface controls the growth of face {011}, as also indicated by Eq. (3).

The fitting of the growth rate in the {10-1} face direction, G_2, corresponds to a birth and spread (B&S) growth mechanism (Eq. (S.2)) with the following equation:

$$G_2 = G\{10-1\} = \frac{S-1.01}{9.54\times10^{-3}+\frac{1}{4.0\times10^{4}\times(S-1.01)^{-1/6}\times exp\left(\frac{0.5}{S-1.01}\right)}} \quad (4)$$

As both the diffusion related term and surface integration term have similar values (see Eq. (4)), the diffusion (mass transfer) and surface integration have the similar effect on the crystal growth of face {10-1}.

It was found that the growth of α-*p*ABA crystals in the {101} face direction was too slow to measure directly and thus the {101} face growth rate, G_1, was estimated from G_2 based on the ratio of attachment energies between face {101} and face {10-1} (Rosbottom et al., 2015). Hence

$$G_1 = G\{101\} = 0.1 * G_2 \quad (5)$$

4.2 Base Case

Figure 4 shows the simulated solution temperature, supersaturation, crystal concentration, mean normal distances (x_1, x_2, x_3) for faces {101}, {10-1}, {011}, and the corresponding facet growth rates at a cooling rate (*CR*) of 0.5°C/min. The mean normal distance for face {011} increased rapidly with time as the face {011} is the fastest growing face from previous studies (Rosbottom et al., 2015, Toroz et al., 2015), while less growth happened in *x* direction.

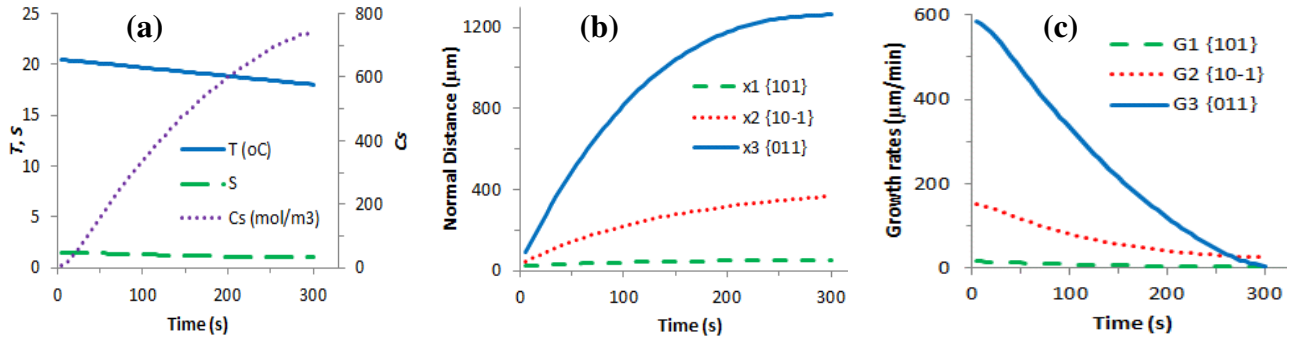

364

365 **Figure 4.** Typical MPB predicted results with CR = 0.5°C/min: (a) solution temperature (T),
366 supersaturation (S), crystal concentration (Cs), (b) evolution of mean normal distances (x_1, x_2, x_3), and
367 (c) facet growth rates (G_1, G_2, G_3) in (x_1, x_2, x_3) face directions.

368

369 Figure 5 presents the typical shape distribution of α-*p*ABA crystals in the final product with a fixed
370 normal distance, x_1, of 30.8μm, and other two normal distances (x_2, x_3) varying from (45 μm, 105
371 μm) to (163 μm, 262 μm). For each normal distances of (30.8, x_2, x_3), the corresponding crystals
372 shape can be generated based on the definition in Figure 2(b). Therefore, the crystal shape and the
373 number of crystals having this shape were plotted in Figure 5. It demonstrated that the simulated
374 results can provide the accurate and full shape information of the whole population of the crystals.
375 Similarly, the full shape information can be obtained from the simulation results at any individual
376 crystallisation time. Therefore, the evolution map of crystal shape over the whole crystallisation
377 process can be established. Some crystal mean shapes at different processing times are plotted in
378 Figure 6. Due to the fast growth of face {011}, the α-*p*ABA crystals became increasingly needle-like
379 with time. The aspect ratio, X_3/X_2 (where X_2 and X_3 are the mean values of x_2, x_3 at a crystallisation
380 time), increased from 2.2 (seeds) to 5.3, then reduced slightly to 4.8 (final products). This is due to
381 that the faceted growth rates of face {011}, G_3, and face {10-1}, G_2, have a cross-over at the
382 supersaturation of 1.18, i.e. with the further decrease of supersaturation from 1.18, G_3 became smaller
383 than G_2. Similar tread was found for the aspect ratio, X_3/X_1 (where X_1 is the mean value of x_1), with a
384 much faster increase against time due to that the x_1 grew very slow. Therefore the aspect ratio (X_3/X_1)
385 increases from 6 to over 30.

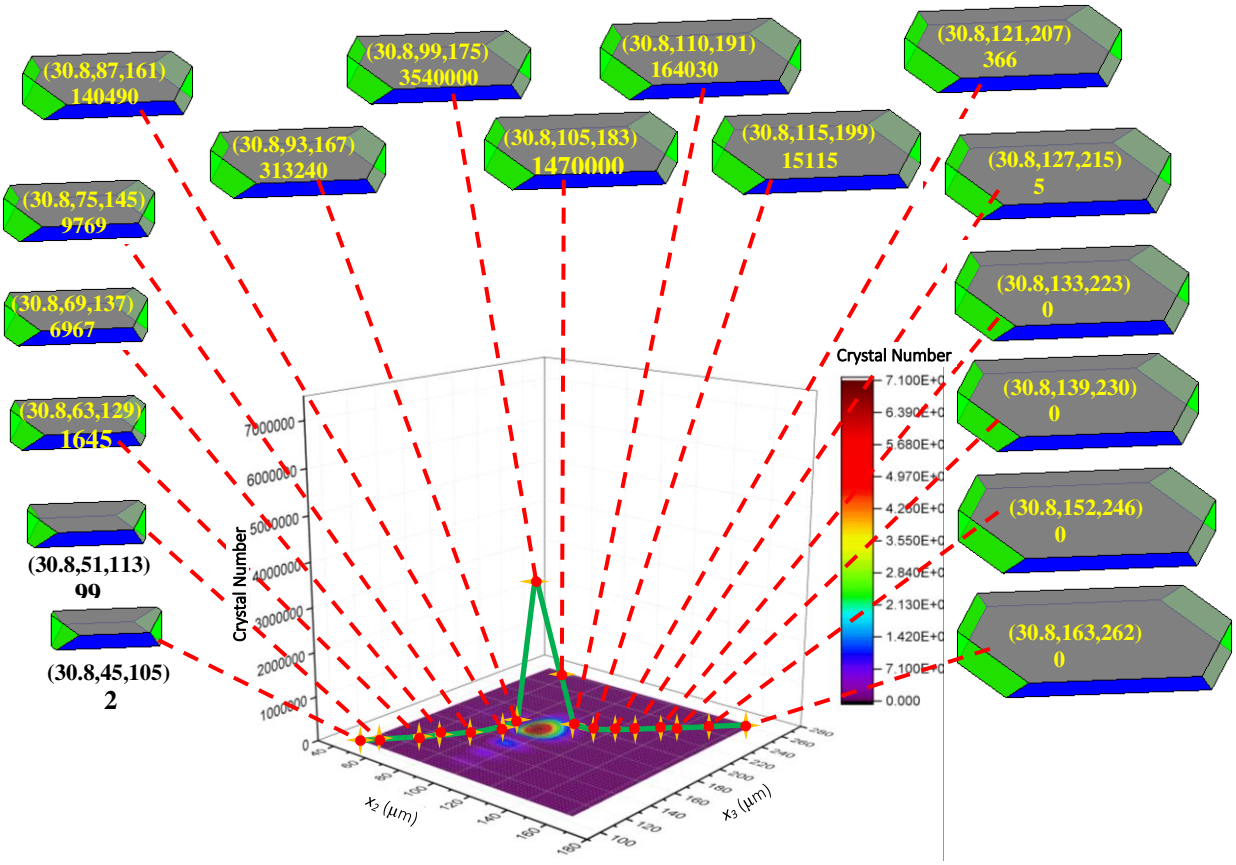

386

387 **Figure 5.** Typical shape distribution of α-*p*ABA crystals with a fixed normal distance, x_1, of 30.8
388 μm, and other two normal distances (x_2, x_3) varying from (45 μm, 105 μm) to (163 μm, 262 μm).
389 Note that the values in the brackets are the three normal distances for the individual crystal habit faces
390 (x_1, x_2, x_3) in micrometres together with the number under the brackets which gives the number of
391 crystals having this specified shape as defined by the normal distances.

392

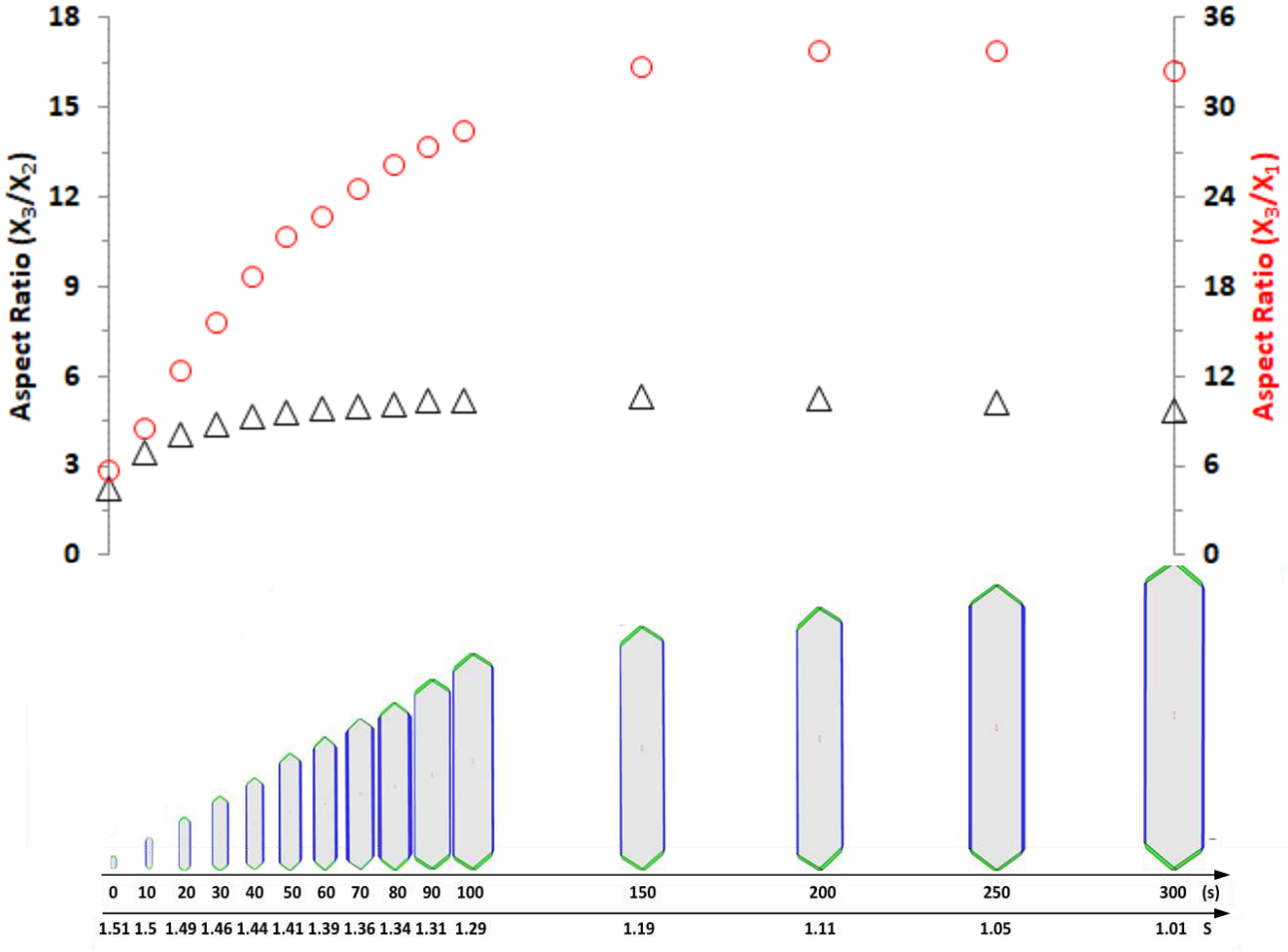

Figure 6. MPB predicted mean shape evolution of α-*p*ABA crystals crystallised from ethanol with *CR* = 0.5°C/min (Aspect ratios: △ - X_3/X_2; ○ - X_3/X_1).

4.3 Effect of Cooling Rate

Figure 7 shows the evolution of supersaturation during crystallisation processes (Figure 7a), and the final shape/size and their corresponding aspect ratios under four cooling rates (Figure 7b). It can be seen that the supersaturation decrease with processing time is slower with higher cooling rate (Figure 7a). As the supersaturation is defined as the ratio between solute concentration in the crystalliser at a given time (temperature) and the solubility of the solute-solvent system at the same given time (temperature), the evolution of supersaturation during a crystallisation process can be fast or slow depending on the balance of the solute concentration and solubility. In this study, the higher cooling rate led to faster decrease of solubility (due to the faster decrease of temperature) than the lower cooling rate. However, the decrease of solute concentration (due to crystal growth, hence consuming solute in the solution) does not necessarily follow the same decrease speed. Therefore, if the decrease of solute concentration is slower that the solubility, the combining effects could result in the slower

reduction of supersaturation with higher cooling rate. The final shape/size under various cooling rates was found to be similar and the corresponding aspect ratio (X_3/X_2) varied between 4.8 and 4.3 (Figure 7b), which indicates that the variation of cooling rate may not be an effective tool to manipulate crystal size/shape of final products under the current operating conditions.

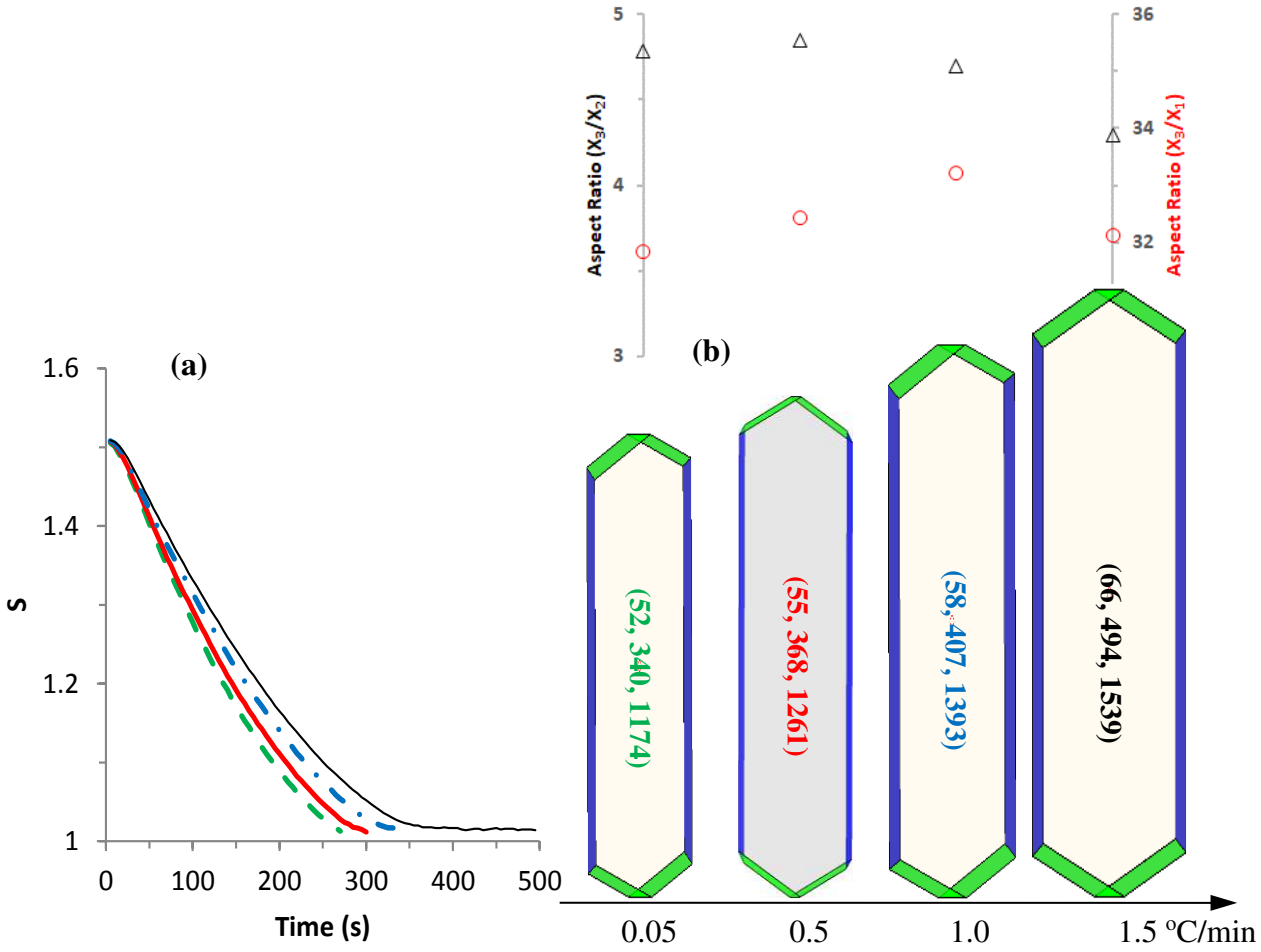

Figure 7. (a) Supersaturation evolution during crystallisation processes and (b) final mean shape/size under different cooling rate (*CR* = 0.05°C/min – dash green line; *CR* = 0.5°C/min – red line; *CR* = 1.0°C/min – dash and dot blue line; *CR* = 1.5°C/min – black line).

Figures 8 and 9 illustrate the evolution of faceted growth rates and normal distances, respectively, during crystallisation processes in face direction of {101}, {10-1} and {011} under different cooling rates. The face-specific growth rates of the three faces decreased during the process with the speed of decrease being slower at higher cooling rate. The corresponding normal distances for all three faces increased faster with the higher cooling rate. By examining the final size/shape of α-*p*ABA crystals with various cooling rates when supersaturation researched a value of 1.01 (hence no further crystallisation), the total crystallisation time, final temperature, total crystal mass (yield) and the fine

mean size/shape were obtained as shown in Table 2. The total crystal mass in Table 2 was obtained from $\rho_s \sum_{i=1}^{N_1} \sum_{j=1}^{N_2} \sum_{k=1}^{N_3} [V(x_{1,i}, x_{2,j}, x_{3,k})\ \Phi(x_{1,i}, x_{2,j}, x_{3,k})]$, where ρ_s is the density of the crystal, $V(x_{1,i}, x_{2,j}, x_{3,k})$ is the volume of a crystal with normal distances of $(x_{1,i}, x_{2,j}, x_{3,k})$ calculated based on the crystals shape shown in Figure 2(b) and $(x_{1,i}, x_{2,j}, x_{3,k})$, and the definitions of other variables can be found in the Supplementary materials (S3). With the increase of cooling rate from 0.05 to 1.5°C/min in this study, the total process time is almost doubled with the corresponding final temperature being lowered from about 20°C to 8°C and the yield of α-*p*ABA crystals being increased about 50%. Furthermore the final crystal size is about 40% larger with *CR* = 1.5°C/min than 0.05°C/min though the variation of final crystal mean shape (aspect ratio) is not significant.

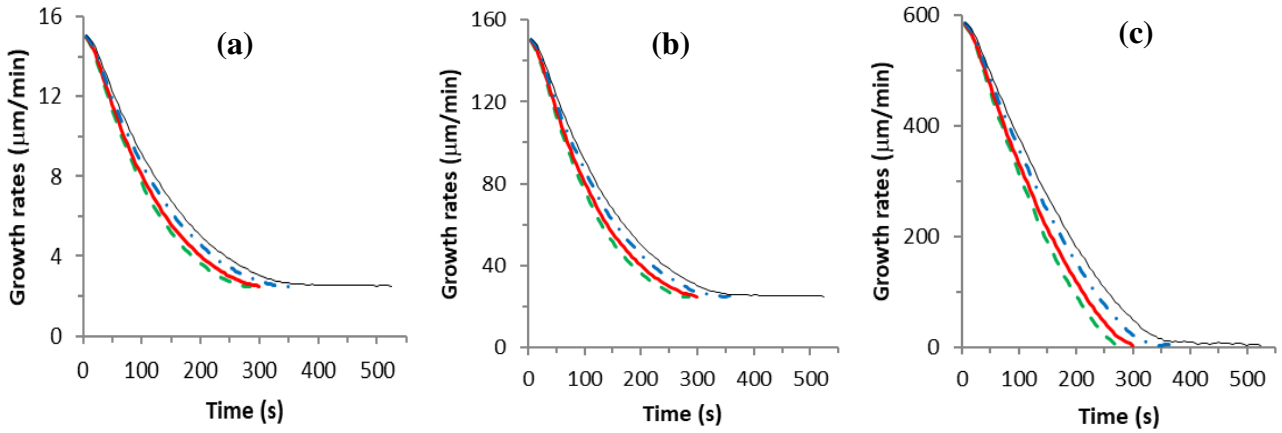

Figure 8. Evolution of faceted growth rates during crystallisation processes in face direction of (a) face {101}, (b) face {10-1} and (c) face {011} under different cooling rate (*CR* = 0.05°C/min – dash green line; *CR* = 0.5°C/min – red line; *CR* = 1.0°C/min – dash and dot blue line; *CR* = 1.5°C/min – black line).

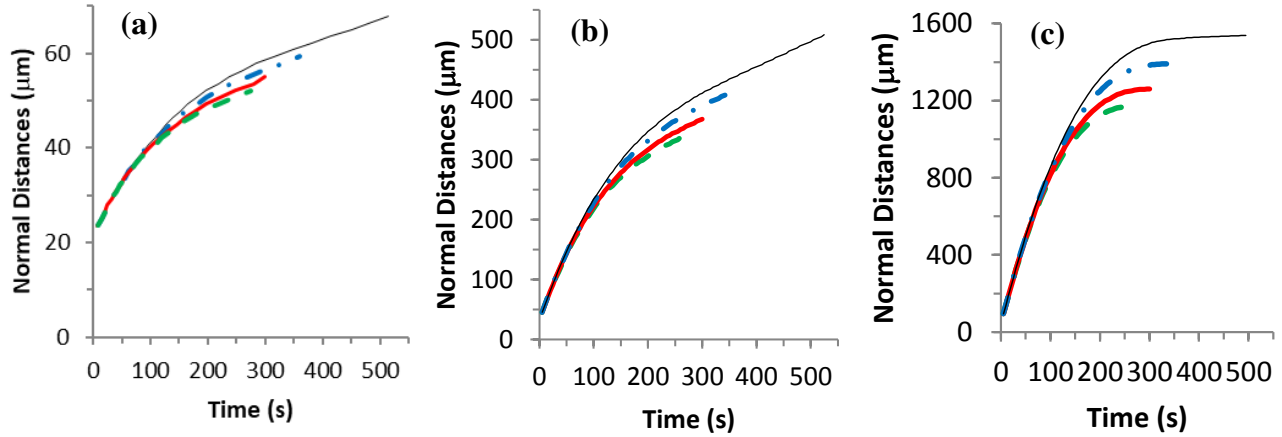

Figure 9. Evolution of normal distances during crystallisation processes in face direction of (a) face {101}, (b) face {10-1} and (c) face {011} under different cooling rate (*CR* = 0.05°C/min – dash green

line; CR = 0.5°C/min – red line; CR = 1.0°C/min – dash and dot blue line; CR = 1.5°C/min – black line).

Table 2. MPB modelling results of α-*p*ABA crystallised from ethanol under different CR

CR (°C/min)	Process Time (s)	Final S (-)	Final T (°C)	Final mean (x_1, x_2, x_3) (μm)	Total crystal – mass (g)
0.05	270	1.01	20.3	52, 340, 1174	50.7
0.5	300	1.01	18.0	55, 368, 1261	55.0
1.0	340	1.01	14.8	58, 409, 1393	60.5
1.5	495	1.01	8.2	66, 495, 1539	73.1

4.4 Effect of Seeding Temperature

In order to investigate the effect of seeding temperature on seeded cooling crystallisation of α-*p*ABA in a batch crystalliser, the seeding temperature (T_{seeds}) was varied from 20.5°C to 39.0°C, which corresponds to seeding supersaturation (S_{seeds}) decreasing from 1.5 to 1.1. The supersaturation evolution during crystallisation processes and the final mean shape/size under different seeding temperature (or seeding supersaturation) are plotted in Figure 10. With a fixed cooling rate of 0.5°C/min, as shown in Figure 10a, the supersaturation decreased much faster with lower T_{seeds} (or higher S_{seeds}) than higher T_{seeds} (or lower S_{seeds}). The total process time for various T_{seeds} (or S_{seeds}) did not show significant variation (Table 3). From Figure 10b, it is clear that final mean crystal size with higher T_{seeds} (or lower S_{seeds}) is smaller in size and less needle-like in shape (or lower aspect ratio) (Table 3). When varying of S_{seeds} from 1.1 to 1.5, the aspect ratio (X_3/X_2) was increased from 2.5 to 4.8 (Figure 10b).

For the evolution of face-specific growth rates and normal distances (x_1, x_2, x_3), respectively, during crystallisation processes in face direction of {101}, {10-1} and {011} under different T_{seeds} (or S_{seeds}), the supersaturation decreased slower with higher T_{seeds} (or lower S_{seeds}), hence the facet growth rates for the three individual faces followed the same trend (Figure S.1 in Supplementary materials (S4)). Correspondingly, the normal distances (x_1, x_2, x_3) increased against crystallisation time much faster with lower T_{seeds} (or higher S_{seeds}) and also larger actual normal distances (Figure S.2 in Supplementary materials (S4)). Furthermore, this is more significant for the evolution of normal distance of face {011}, i.e. x_3. As a result, the higher growth rates and bigger actual normal distances with lower T_{seeds} (or higher S_{seeds}) produced much higher yield as shown in Table 3. Therefore, it is not optimal to select an experiment with higher T_{seeds} (or lower S_{seeds}) as the resultant yield would be

unacceptably low albeit from these conditions the final crystal shape would be expected to be less needle-like (smaller aspect ratio).

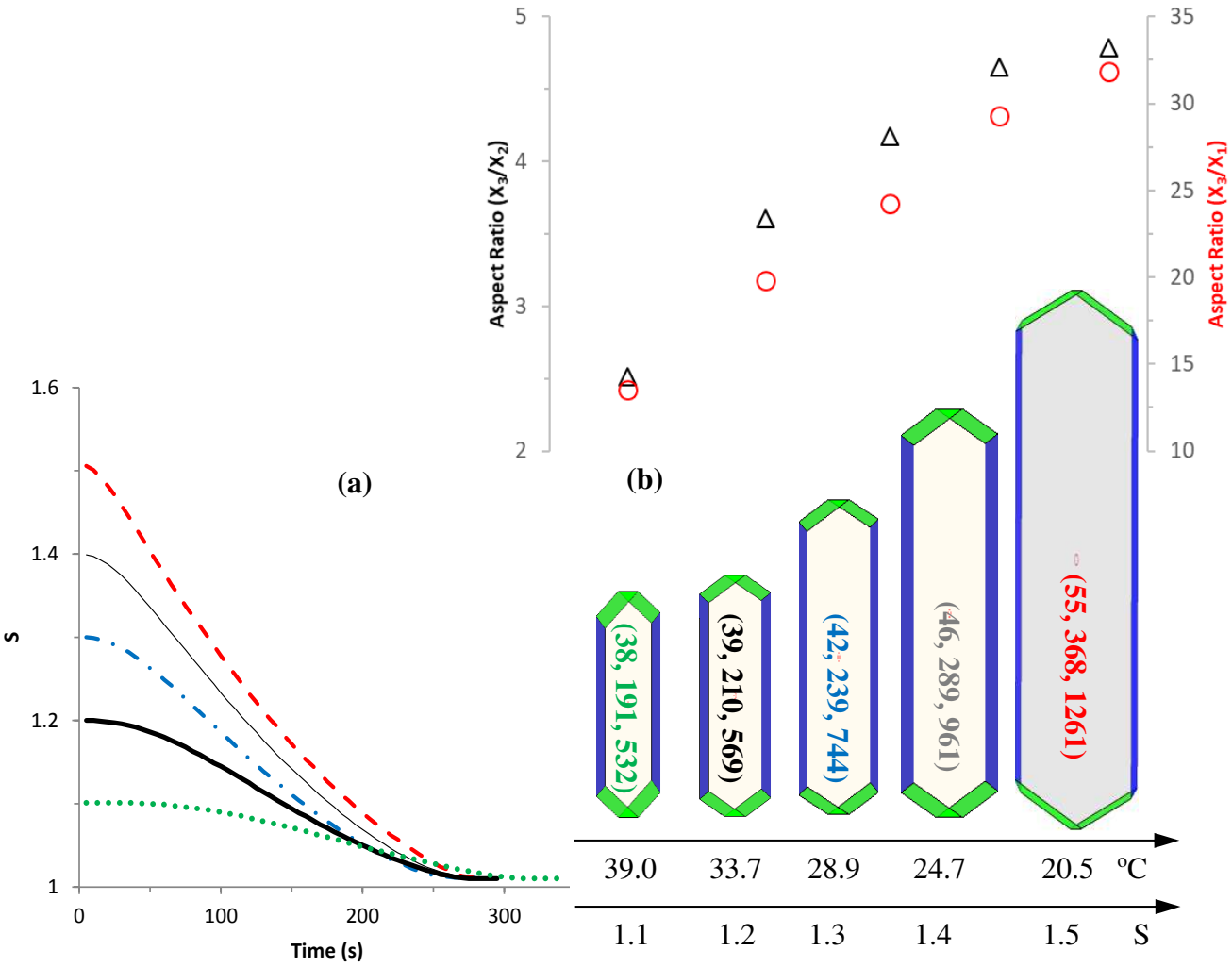

Figure 10. (a) Supersaturation evolution during crystallisation processes and (b) final mean shape/size under different seeding temperature (T_{seeds}) (or supersaturations (S_{seeds})) (T_{seeds} = 20.5°C (or S_{seeds} = 1.5) – dash red line; T_{seeds} = 24.7°C (or S_{seeds} = 1.4) – thin black line; T_{seeds} = 28.9°C (or S_{seeds} = 1.3) – dash and dot blue line; T_{seeds} = 33.7°C (or S_{seeds} = 1.2) – black line; T_{seeds} = 39.0°C (or S_{seeds} = 1.1) – dot green line).

Table 3. MPB modelling results of α-*p*ABA crystallised from ethanol under different seeding temperature (T_{seeds}) (or seeding supersaturation (S_{seeds}))

Seeding point – T_{seeds} (°C)	**S_{seeds} (-)**	**Time (s)**	**Final S (-)**	**Final T (°C)**	**Final means (x_1, x_2, x_3) (μm)**	**Total crystal – mass (g)**
39.0	1.1	290	1.01	36.55	37.9, 191, 376	17.5
33.7	1.2	260	1.01	31.5	39.3, 210, 568	28.5
28.9	1.3	250	1.01	26.85	42.1, 239, 744	38.0
24.7	1.4	265	1.01	22.47	46.4, 289, 961	46.5
20.5	1.5	300	1.01	18.0	55, 368, 1261	55.0

4.5 Effect of Seed Loading

Figure 11 shows the evolution of supersaturation during crystallisation processes (Figure 11a), and the final mean shape/size and their corresponding aspect ratios (Figure 11b) under five different seed loadings. With higher seed loading under the same Gaussian-like size/shape distribution (same mean values and same standard deviations), the total number of crystals becomes proportionally larger. Therefore, the total crystal surface area for crystal growth is predicted to increase with the increase of seed loading, hence solute concentration reduces faster, leading to faster supersaturation decrease (Figure 11a). As the total number of seeds is higher with higher seed loading, the solute available for each seed is less accordingly. Therefore, as shown in Figure 11b, the final mean crystal is smaller in size and also less needle-like in shape (or aspect ratio). When seed loading increases from 0.1% to 2.0% (by mass), the MPB simulation results show that the aspect ratio (X_3/X_2) decreases almost linearly with a slope of -0.4 and intercept of 4.8 (Figure 11b).

The evolution of faceted growth rates (Figure S.3 in Supplementary materials (S5)) and face normal distances (Figure S.4 in Supplementary materials (S5)) during crystallisation processes on the {101}, {10-1} and {011} faces under different seed loadings demonstrated that as the increase of seed loading resulted in the faster decrease of supersaturation (Figure 11a), the faceted growth rates (G_1, G_2, G_3) also decrease faster (Figure S.3) with the corresponding normal distances being in slower increase (Figure A.4). The final temperature and yield did not have significant variation for the simulated range of seed loadings (Table 4). However, the crystal size of final product is predicted to be smaller with less needle-like in shape when seed loading is increased. Therefore, seed loading can be an effective tool for optimising and controlling crystal size/shape distribution using MPB approach.

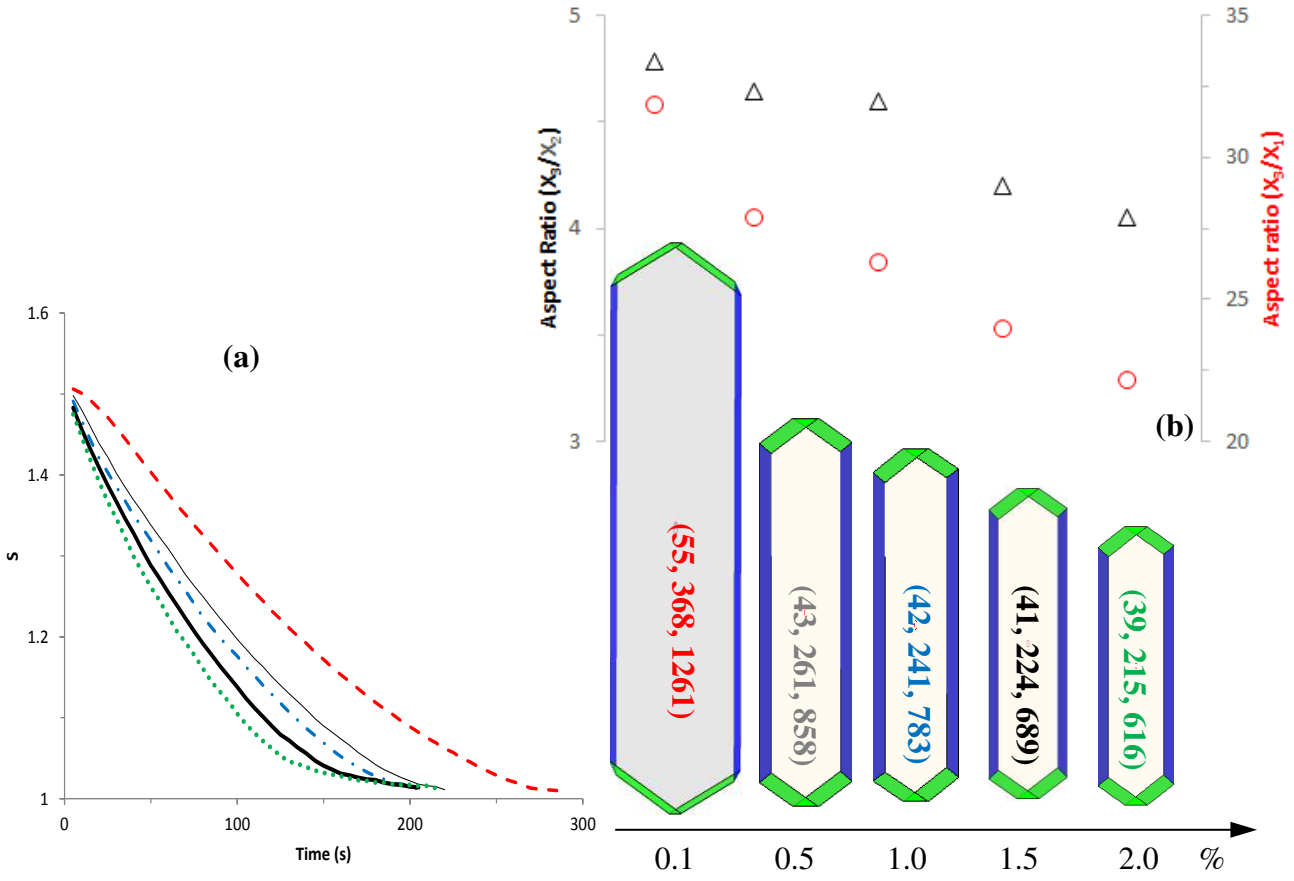

509

510 **Figure 11.** (a) Supersaturation evolution during crystallisation processes and (b) final mean
511 shape/size under different seed loading (X_{seeds}) (X_{seeds} = 0.1% – dash red line; X_{seeds} = 0.5% – thin
512 black line; X_{seeds} = 1.0% – dash and dot blue line; X_{seeds} = 2.0% – black line; X_{seeds} = 5.0% – dot green
513 line).

514

515 **Table 4.** MPB modelling results of α-*p*ABA crystallised from ethanol under different seed loading
516 (X_{seeds})

X_{seeds} (% mass)	Time (s)	Final S (-)	Final T (°C)	Final means (x_1, x_2, x_3) (μm)	Total crystal – mass (g)
0.1	270	1.01	18.0	55, 368, 1261	55.0
0.5	220	1.01	18.7	43.6, 261, 858	54.5
1.0	205	1.01	18.8	42.1, 241, 783	55.0
2.0	205	1.01	18.8	40.7, 224, 689	56.3
5.0	215	1.01	18.7	39.3, 215, 616	57.4

517

518

519

4.6 Effect of Seed Mean Shape

To investigate the effect of seed mean shape on crystal size/shape distribution during α-*p*ABA crystallisation process, three different mean shape were used for establishing seeds size/shape distribution (e.g. Figure 3a): mean normal distances (x_1, x_2, x_3) of (22, 27, 6 μm), (22, 27, 40 μm) and (22, 27, 131 μm) with fixed standard deviations of $(\sigma_{x_1}, \sigma_{x_2}, \sigma_{x_3})$ = 8 μm. Figure 12 shows the supersaturation evolution during crystallisation processes and the final mean shape/size under different seed mean shape. With more needle-like seeds, the total number of seeds (under the same seed loading) was found to be slightly smaller, hence leading to slower decrease of supersaturation (Figure 12a). However, the simulated final crystal size is found to be bigger with slightly higher aspect ratio (Figure 12b). Similarly, the faceted growth rates follow the same trend of decrease (Figure S.5 in Supplementary materials (S6)) and the normal distances (x_1, x_2, x_3) have the similar trend of increase with crystallisation time (Figure S.6 in Supplementary materials (S6)). The final temperature and yield do not present significant variation for the three seed mean shape (Table 5).

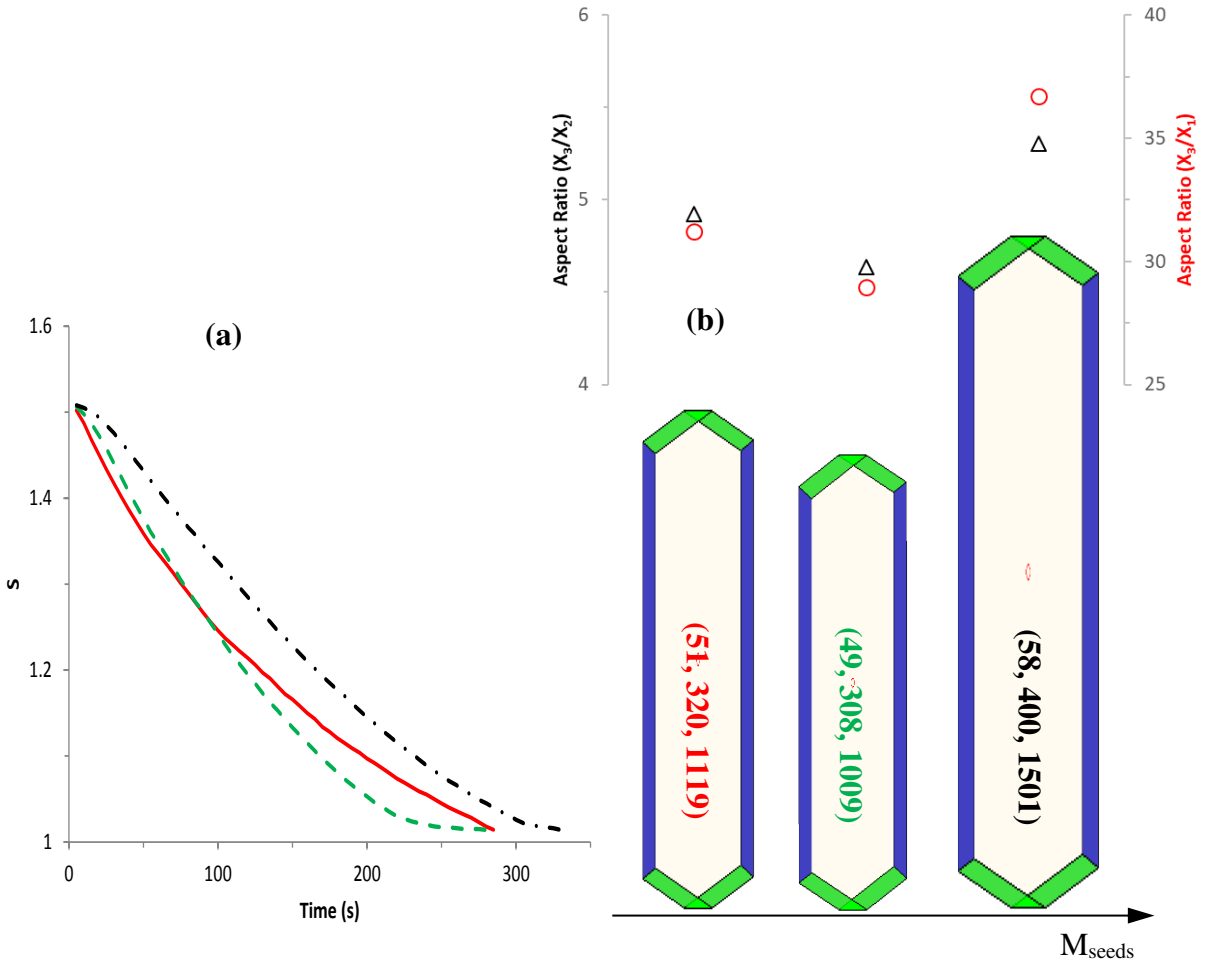

Figure 12. (a) supersaturation evolution during crystallisation processes and (b) final mean shape/size under different seed mean shape (M_{seeds}) with standard deviations of $(\sigma_{x_1}, \sigma_{x_2}, \sigma_{x_3})$ = 8 μm (M_{seeds} =

(22, 27, 6 μm) – red line; M_{seeds} = (22, 27, 40 μm) – dash green line; M_{seeds} = (22, 27, 131 μm) – dash and dot black line).

Table 5. MPB modelling results of α-*p*ABA crystallised from ethanol under different seed mean shape (M_{seeds})

M_{seeds} (x_1, x_2, x_3) (μm)	Seeds standard deviations ($\sigma_{x_1}, \sigma_{x_2}, \sigma_{x_3}$) (μm)	Time (s)	Final S (-)	Final T (°C)	Final means (x_1, x_2, x_3) (μm)	Total crystal – mass (g)
22, 27, 6	8, 8, 8	285	1.01	18.1	50.7, 320, 1119	54.6
22, 27, 40	8, 8, 8	280	1.01	18.18	49.3, 308, 1009	54.4
22, 27, 131	8, 8, 8	330	1.01	17.76	57.9, 400, 1501	55.2

4.7 Effect of Broken Seeds

Theoretically seeds may be treated as prefect crystals with the required size/shape distribution. However, in practice, seeds are usually collected from small scale and well-controlled crystallisation processes, then followed by the necessary washing, filtration and drying, all processes which might expect to provide some extent of breakage/damage to the obtained seeds. In order to obtain seeds with the required size, milling/sieving processes may be used, which understandably will generate broken seeds at very high extent. In this section, the MPB model was used to simulate the behaviour of the broken seeds during crystallisation processes. All operating conditions are as the same as those from the base case (section 4.2) with the size/shape distribution of broken seeds as shown in Figure 3b. The broken face (010) should be rough with most possibly an RIG growth mechanism. In this study, the facet growth rate of face (010) was estimated to be two times of that for face {011}, G_3. It should be noted that the more accurate growth rate and growth mechanism for the broken face (010) are needed through the use of molecular modelling and/or experimental measurements.

Figure 13 shows the solution temperature, supersaturation, solute concentration and solid concentration during crystallisation processes with perfect seeds or broken seeds. With the same cooling rate (0.5°C/min), supersaturation with broken seeds decreased slightly faster, hence reaching the supersaturation value of 1.01 earlier (~ 28s). Correspondingly, solute concentration dropped at a higher speed and solid concentration increased faster.

Figures 14 presents the faceted growth rates in the directions of faces {101}, {10-1} and {011}, and also broken face (010) with its trajectory, and the corresponding evolution of normal distances for the mentioned four faces. MPB simulations revealed that the broken face (010) grew very fast, then

disappeared after about 15 s (Figure 14b). The facet normal distances, in particular x_3 for face {011}, increased slower at the late stage of the crystallisation process with broken seeds. The main contributors are both broken seeds (shorter in size and higher number of seeds) and the faster decrease of supersaturation (also faster decrease of growth rate of face {011} (Figure 14a)).

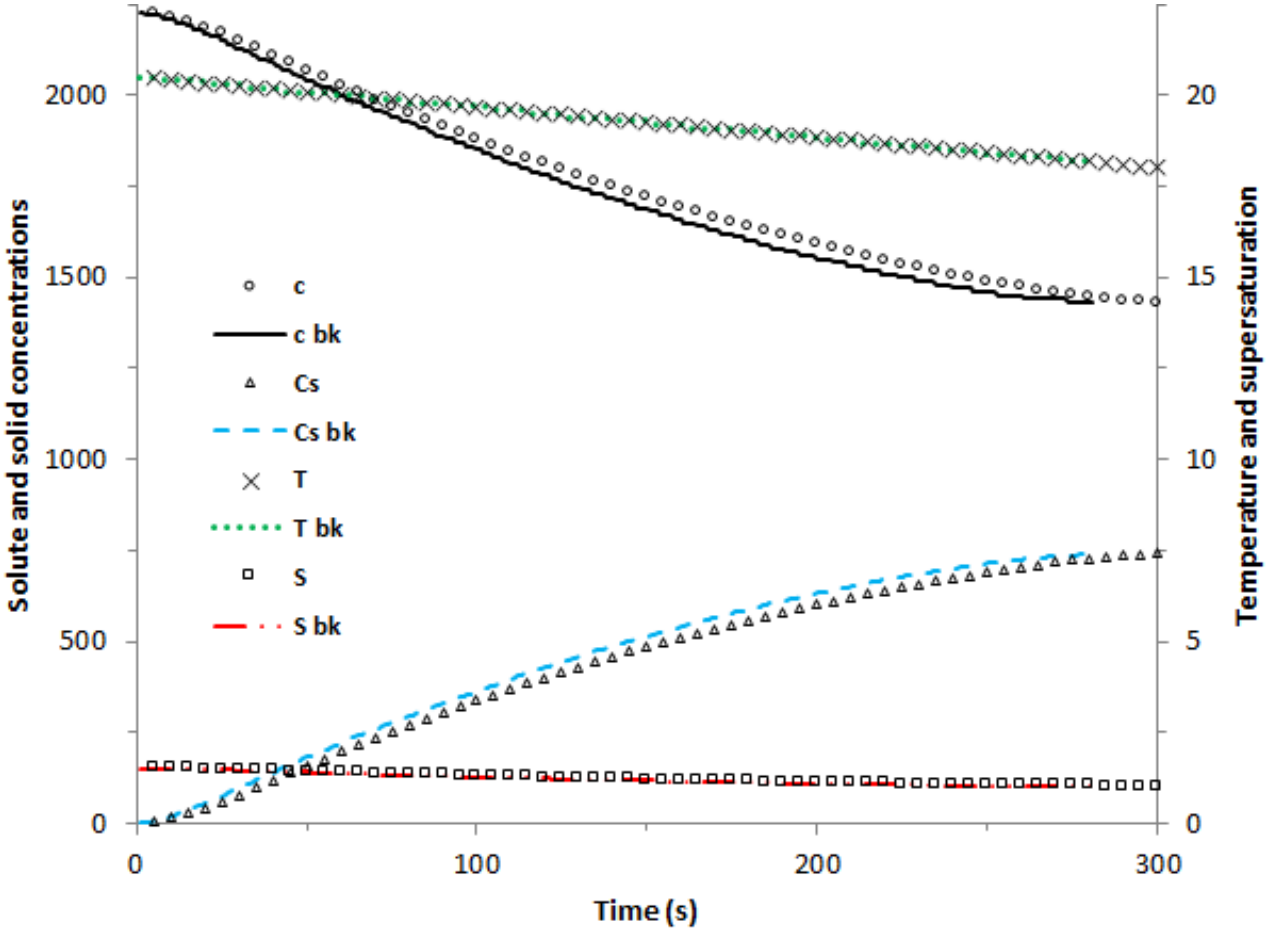

Figure 13. Solution temperature (T and T_{bk}), supersaturation (S and S_{bk}), solute concentration (c and c_{bk}) and solid concentration (Cs and Cs_{bk}) during crystallisation processes with the operating conditions of the base case and broken seeds (Symbols – perfect seed crystals; Lines – broken seed crystals; bk – broken seeds).

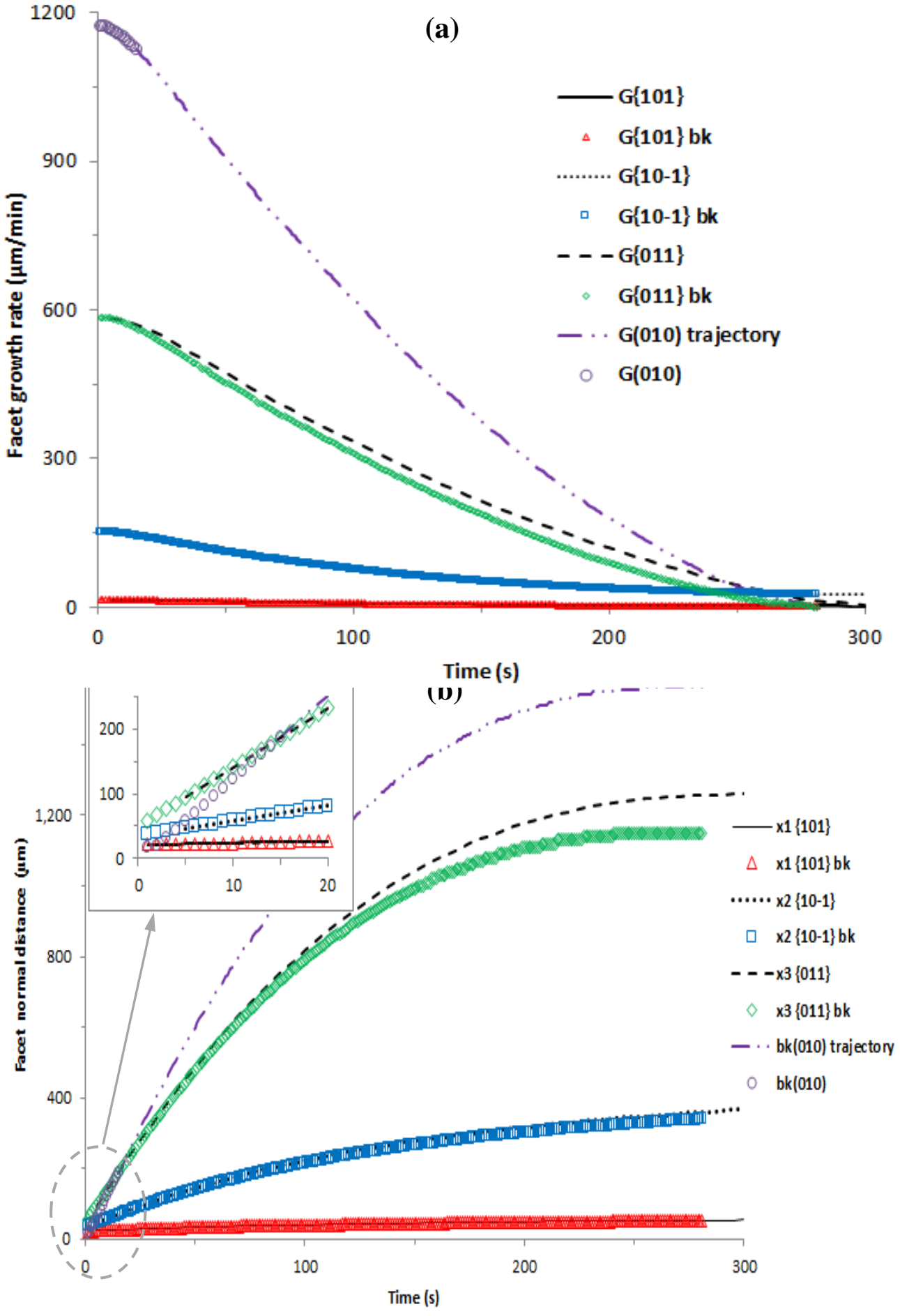
(a)
Facet growth rate (μm/min)
Time (s)
G{101}
G{101} bk
G{10-1}
G{10-1} bk
G{011}
G{011} bk
G(010) trajectory
G(010)
(b)
Facet normal distance (μm)
Time (s)
x1 {101}
x1 {101} bk
x2 {10-1}
x2 {10-1} bk
x3 {011}
x3 {011} bk
bk(010) trajectory
bk(010)

572

573 **Figure 14.** Faceted growth rates (a) and Normal distances (b) in the face directions of face {101}
574 (solid line – perfect seed crystals; △ – broken seed crystals), face {10-1} (dot line – perfect seed
575 crystals; □ – broken seed crystals) and face {011} (Dash line – perfect seed crystals; ◇ – broken
576 seed crystals), and also broken face (010) (dash and dots line) with its trajectory (○) during
577 crystallisation processes with the operating conditions of the base case.

578

579 Figures 15 and 16 present the evolution of aspect ratios (X_3/X_2, X_3/X_1, X_2/X_1) during crystallisation
580 process for both prefect seeds and broken seeds, and crystal mean shape evolution and aspect ratios
581 at several typical time points for broken seeds, respectively. Note that X_1, X_2 and X_3 are the mean
582 values of x_1, x_2, x_3 at a crystallisation time. The aspect ratios (X_3/X_2 and X_3/X_1) increased fast to the
583 values for prefect seeds after about 15 s (Figure 15) with the broken face (010) being disappearance
584 (Figure 16).

585

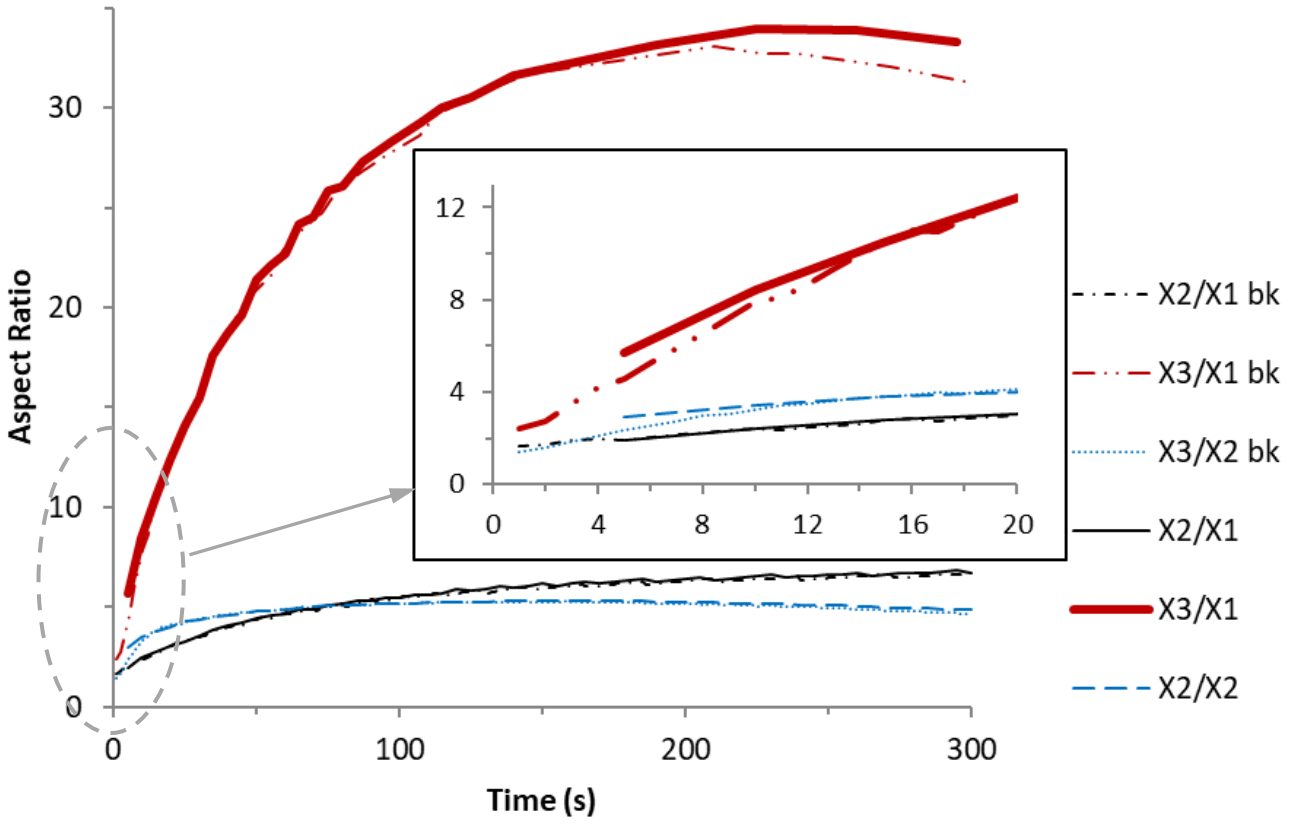

586 **Figure 15.** Evolution of aspect ratios during crystallisation process with prefect and broken seeds.

587

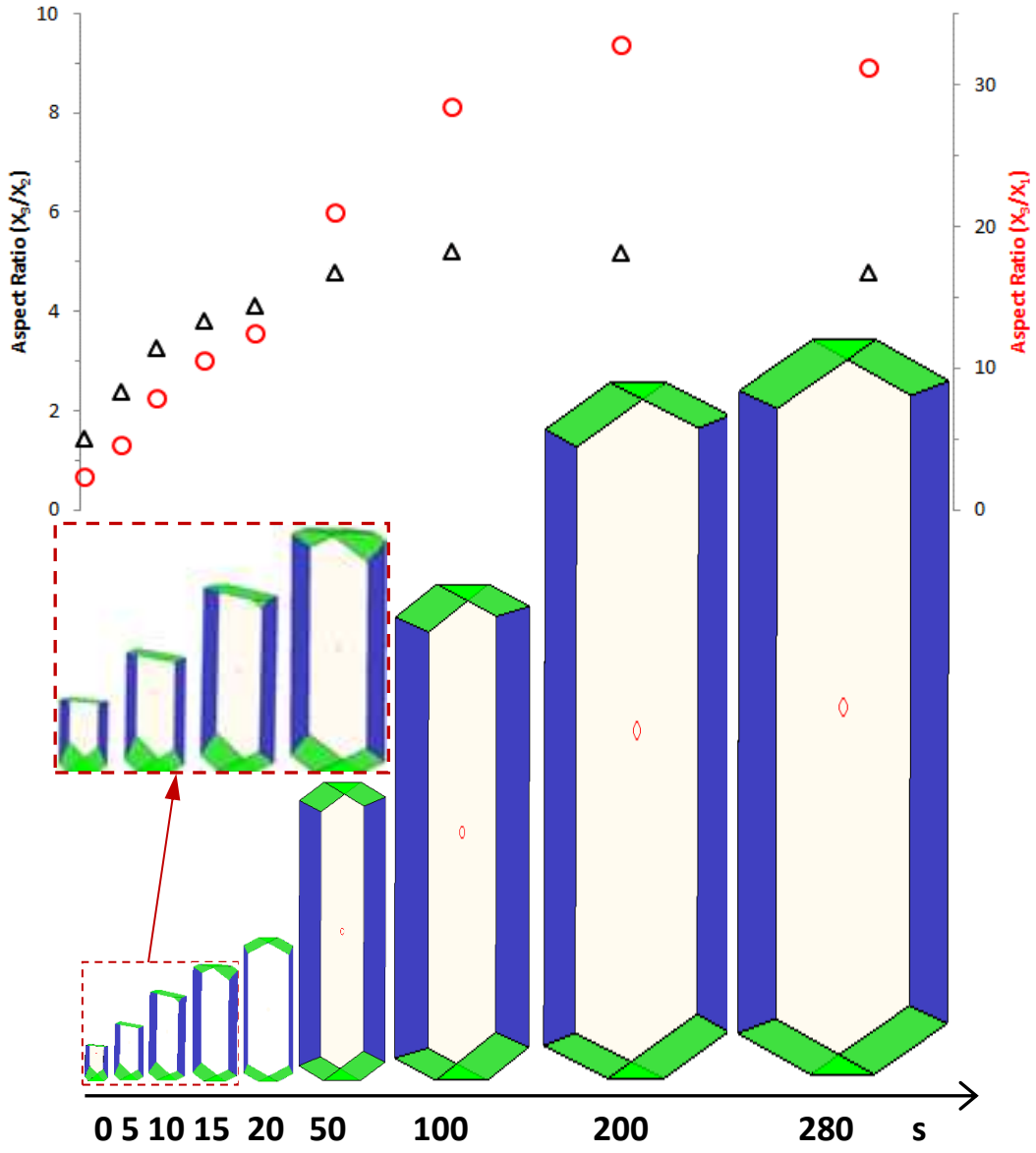

588

589 **Figure 16.** Crystal mean shape evolution and aspect ratios at some typical time instances (0, 5, 10,
590 15, 20, 50, 100, 200, 300 s). Note that the broken face (010) grew fast and disappeared in about 15 s.

591

592 **5. Conclusions**

593 In this study, the MPB models were applied for simulating pharmaceutical crystallisation processes
594 as illustrated through a case study of α-*p*ABA crystals crystallised from ethanolic solution under a
595 wide-range of operating conditions notably cooling rate, seeding temperature (seeding
596 supersaturation), seed loading, seeds shape/size (including broken seeds). The MPB simulations
597 captured the shape-dependent behaviour of the crystallisation processes under these operating
598 conditions with the effect of defining the impact of these processing variables on the crystal size/shape
599 distribution and their evolution.

Within the operating conditions used for MPB simulations, faster cooling was shown to increase the crystallisation time to reach solution equilibrium conditions, i.e. S = 1, with the corresponding finishing solution temperature being much lower, hence leading to higher yield and larger final crystal size. Although higher seeding temperatures (hence lower seeding supersaturations) was found to produce less needle-like α-*p*ABA crystals, the yield was much lower than that at lower seeding temperatures. On the other hand, higher seed loading was found to generate smaller sized crystals which were less needle-like in shape while having very similar yields. This indicated that seed loading could be a useful control variable for using MPB to obtain the pre-desired crystal size/shape distribution. For the case with broken seeds, the fractured seed surfaces were found to grow fast and hence disappear from the external morphology during the crystallisation process. Such simulations could have wide applications in pharmaceutical industry mindful that seeds used often exhibit some kind of breakage and/or damage during seed preparation processes, e.g. through milling.

Further research should include the consideration of the effect of primary nucleation (i.e., without seeds) and together with that of secondary nucleation through surface breeding from seeds, face-specific crystal agglomeration and breakage into the MPB model. This will involve first-principle based research on crystal morphology and surface chemistry, solid/solution interface (including the interactions of crystal-crystal, crystal-solute and crystal-solvent), solution chemistry, etc. Through these, combining the MPB model with computational fluid dynamics for crystalliser hydrodynamics and multi-zonal modelling will form a powerful digital design framework for pharmaceutical crystallisation to manufacture crystals with pre-desired properties, hence delivering targeted medicines.

Acknowledgments

The authors gratefully acknowledge the financial support by the UK´s Advanced Manufacturing Supply Chain Initiative 'Advanced Digital Design of Pharmaceutical Therapeutics' (ADDoPT) project (Grant No. 14060). This work also builds upon research on morphological modelling supported by EPSRC grant 'HABIT – Crystal morphology from crystallographic and growth environment factors' through EPSRC grant EP/I028293/1 and the Synthonic Engineering programme supported by Pfizer, Boeringer-Ingellheim, Novartis and Syngenta. We also gratefully acknowledge EPSRC for the support of crystallization research at Leeds and Manchester through the Critical Mass grant 'Molecules, Clusters and Crystals' (Grant references EP/IO14446/1 and EP/IO13563/1).

Declarations of interest: none

References

BELL, J. 2017. Life Sciences Industrial Strategy - A report to the Government from the life sciences sector (https://www.gov.uk/government/publications/life-sciences-industrial-strategy).

CAMACHO, D. M., ROBERTS, K. J., MULLER, F., THOMAS, D., MORE, I. & LEWTAS, K. 2016. Morphology and Growth of Methyl Stearate as a Function of Crystallization Environment. *Crystal Growth & Design,* 17**,** 2088-2095.

CLYDESDALE, G., DOCHERTY, R. & ROBERTS, K. J. 1991. Habit - a program for predicting the morphology of molecular-crystals. *Computer Physics Communications,* 64**,** 311-328.

CLYDESDALE, G., ROBERTS, K. J. & DOCHERTY, R. 1996. HABIT95, Quantum Chemistry Program Exchange, Program no. 670, Bloomington, IN 47405, USA.

HULBURT, H. M. & KATZ, S. 1964. Some Problems in Particle Technology - a Statistical Mechanical Formulation. *Chemical Engineering Science,* 19**,** 555-574.

KUVADIA, Z. B. & DOHERTY, M. F. 2013. Reformulating Multidimensional Population Balances for Predicting Crystal Size and Shape. *AIChE Journal,* 59**,** 3468-3474.

LOVETTE, M. A., BROWNING, A. R., GRIFFIN, D. W., SIZEMORE, J. P., SNYDER, R. C. & DOHERTY, M. F. 2008. Crystal Shape Engineering. *Industrial & Engineering Chemistry Research,* 47**,** 9812-9833.

MA, C. Y. & ROBERTS, K. J. 2018. Combining Morphological Population Balances with Face-Specific Growth Kinetics Data to Model and Predict the Crystallization Processes for Ibuprofen. *Ind Chem Eng Res,* 57**,** 16379-16394.

MA, C. Y., WANG, X. Z. & ROBERTS, K. J. 2008. Morphological population balance for modelling crystal growth in individual face directions. *AIChE Journal,* 54**,** 209-222.

MAIER, J. 2017. Made Smarter Review 2017 (https://www.gov.uk/government/publications/made-smarter-review).

MARCHAL, P., DAVID, R., KLEIN, J. P. & VILLERMAUX, J. 1988. Crystallization and precipitation engineering .1. An efficient method for solving population balance in crystallization with agglomeration. *Chemical Engineering Science,* 43**,** 59-67.

NGUYEN, T. T. H., HAMMOND, R. B., ROBERTS, K. J., MARZIANO, I. & NICHOLS, G. 2014. Precision measurement of the growth rate and mechanism of ibuprofen {001} and {011} as a function of crystallization environment. *CrystEngComm,* 16**,** 4568-4586.

PICKERING, J., HAMMOND, R. B., RAMACHANDRAN, V., SOUFIAN, M. & ROBERTS, K. J. 2017. Synthonic Engineering Modelling Tools for Product and Process Design. *In:* ROBERTS, K. J., DOCHERTY, R., TAMURA, R. (ed.) *Engineering Crystallography: From Molecule to Crystal to Functional Form.* Dordrecht: Springer.

PUEL, F., FEVOTTE, G. & KLEIN, J. P. 2003. Simulation and analysis of industrial crystallization processes through multidimensional population balance equations. Part 1: a resolution algorithm based on the method of classes. *Chemical Engineering Science,* 58**,** 3715-3727.

RAMKRISHNA, D. & MAHONEY, A. W. 2002. Population balance modeling. Promise for the future. *Chemical Engineering Science,* 57**,** 595-606.

RANDOLPH, A. D. & LARSON, M. A. 1988. *Theory of particulate processes: Analysis and techniques of continuous crystallization*, Academic Press, London.

ROSBOTTOM, I. 2016. *The Influence of the Intermolecular Synthons on the Molecular Aggregation, Polymorphism, Crystal Growth and Morphology of p-Aminobenzoic Acid Crystals from Solution.* PhD, PhD Thesis, University of Leeds, UK.

ROSBOTTOM, I., MA, C. Y., TURNER, T. D., O'CONNELL, R. A., LOUGHREY, J., SADIQ, G., DAVEY, R. J. & ROBERTS, K. J. 2017. Influence of Solvent Composition on the Crystal Morphology and Structure of p-Aminobenzoic Acid Crystallized from Mixed Ethanol and Nitromethane Solutions. *Crystal Growth & Design,* 17**,** 4151-4161.

ROSBOTTOM, I., ROBERTS, K. J. & DOCHERTY, R. 2015. The solid state, surface and morphological properties of p-aminobenzoic acid in terms of the strength and directionality of its intermolecular synthons. *CrystEngComm,* 17**,** 5768-5788.

SHAMPINE, L. F. & WATTS, H. A. Subroutine RKF45. *In:* G. E. FORSYTHE, M. A. M., C. B. MOLER, ed. Computer Methods for Mathematical Computations, 1977 Englewood Cliffs, N. J.: Prentice-Hall, 135-147.

SULLIVAN, R. A., DAVEY, R. J., SADIQ, G., DENT, G., BACK, K. R., TER HORST, J. H., TOROZ, D. & HAMMOND, R. B. 2014. Revealing the Roles of Desolvation and Molecular Self-Assembly in Crystal Nucleation from Solution: Benzoic and p-Aminobenzoic Acids. *Crystal Growth & Design,* 14**,** 2689-2696.

TOROZ, D., ROSBOTTOM, I., TURNER, T. D., CORZO, D. M. C., HAMMOND, R. B., LAI, X. & ROBERTS, K. J. 2015. Towards an understanding of the nucleation of alpha-para amino benzoic acid from ethanolic solutions: a multi-scale approach. *Faraday Discussions,* 179**,** 79-114.

TURNER, T. D., NGUYEN, T. T. H., NICHOLSON, P., BROWN, G., HAMMOND, R. B., ROBERTS, K. J. & MARZIANO, I. 2019. A temperature-controlled single-crystal growth cell for the in situ measurement and analysis of face specific growth rates. *Journal of Applied Crystallography,* 52**,** 463-467.

ZHANG, Y. C. & DOHERTY, M. F. 2004. Simultaneous prediction of crystal shape and size for solution crystallization. *AIChE Journal,* 50**,** 2101-2112.

Supplementary Materials

This supplementary provides the mini-review of population balance (PB) models (*S1*), face-specific crystal growth kinetics (*S2*), the solution method of morphological PB (*S3*) and the additional simulation results of the evolution of face-specific growth rates and normal distances under different seeding temperature (*S4*), seed loading (*S5*) and seed mean shape (*S6*), and the references for supplementary materials (*S7*).

S1. Mini-review of PB models

For modelling the evolution of a population of crystals during crystallisation processes, one-dimensional (1D) population balance (PB) approach (e.g., (Alvarez and Myerson, 2010, Caillet et al., 2007, Fevotte et al., 2007, Garside, 1985, Gerstlauer et al., 2006, Hounslow et al., 2005, Li et al., 2013, Liu and Li, 2014, Marchal et al., 1988, Menon et al., 2005, Patience et al., 2004, Rawlings et al., 1992, Temmel et al., 2016, Ulbert and Lakatos, 2005, Ward et al., 2006)), using a characteristic size, such as length (e.g., (Vetter et al., 2014, Ward et al., 2011, Zhang and Doherty, 2004)), diameter or radius of a volume equivalent sphere (e.g., (Marchal et al., 1988)) to simplify a faceted crystal, was used and still being used widely. Two-dimensional (2D) PB method was developed to account for needle-/rod-/plate-like crystals (e.g., (Briesen, 2009, Gunawan et al., 2004, Ma et al., 2007, Oullion et al., 2007, Puel et al., 2003a, Puel et al., 2003b, Ramkrishna and Mahoney, 2002, Sato et al., 2008, Shi et al., 2006)), whilst the introducing a volumetric shape factor into the 1D (or 2D) PB is to more accurately represent the crystal volume (Zhang and Doherty, 2004). However, using a 1D PB with the assumptions that all crystal faces have the same surface chemistry, growth mechanism and a constant relative growth rate ratio amongst all faces, the evolution of crystal size and shape could be represented (e.g., Doherty and co-workers (Lovette et al., 2008, Zhang and Doherty, 2004, Kuvadia and Doherty, 2013)). Critically, a 1D PB assumes that the crystal morphology does not change during growth, i.e. that the ratio of the growth rates between the different faces is constant. The aspect was first addressed by Ma et al. (Ma et al., 2008), followed by other researchers (e.g., (Borchert et al., 2009, Borchert and Sundmacher, 2012, Chakraborty et al., 2010, Kwon et al., 2013, Kwon et al., 2014, Liu et al., 2013, Liu et al., 2010b, Liu et al., 2010a, Ma et al., 2016, Ma and Roberts, 2018, Ma and Wang, 2008, Ma and Wang, 2012, Wan et al., 2009, Wang and Ma, 2009, Wang et al., 2008, Majumder and Nagy, 2013, Kuvadia and Doherty, 2013)). A crystal has its face forms identified as $\{hkl\}$. For a cubic crystal, it only has one form but 6 faces. For a potash alum crystal, it has 3 forms but 24 faces. The MPB uses crystal morphology to identify crystal forms with each form being treated as an independent variable (crystal face-to-centre distance) and the total

number of forms determines the number of dimensions of the MPB equation. It can be assumed that the faces of each form have the same surface chemistry, growth mechanism/rate and also other physical/chemical properties. See more detail in e.g. (Ma et al., 2008). The MPB not only provides a direct tool for optimisation and control of both final crystal size and shape but enables control of the particle properties and processing.

S2. Face-specific crystal growth kinetics

The kinetics of a defined crystal growth interface as a function of supersaturation can generally be described by a number of well-known models including power law (Garside, 1985), birth & spread (B&S) and Burton-Cabrera-Frank (BCF) models (Burton et al., 1951). During crystallisation processes in a crystal growth cell and other crystallisers, crystal growth rate is very much a two-step kinetic process encompassing a balance between the incorporation of growth units onto the crystal surface and the diffusion by mass transfer of the growth units within the bulk of the solution (Mullin, 2001, Camacho et al., 2017). The effect of heat transfer on growth rate was also included by (Mersmann et al., 2002). Therefore both factors need to be considered when determining the growth mechanism and can be modelled using the followings (Mullin, 2001, Camacho et al., 2017):

$$G_{power} = \frac{S - S_{crit}}{\frac{\rho_S}{k_{MT}\, C^* M_S} + \frac{1}{k_G (S - S_{crit})^{r-1}}} \quad \text{(S.1)}$$

$$G_{B\&S} = \frac{S - S_{crit}}{\frac{\rho_S}{k_{MT}\, C^* M_S} + \frac{1}{k_G (S - S_{crit})^{-1/6} exp\left(A_1/(S - S_{crit})\right)}} \quad \text{(S.2)}$$

$$G_{BCF} = \frac{S - S_{crit}}{\frac{\rho_S}{k_{MT}\, C^* M_S} + \frac{1}{k_G (S - S_{crit}) tanh\left(A_2/(S - S_{crit})\right)}} \quad \text{(S.3)}$$

Where G_{power}, $G_{B\&S}$ and G_{BCF} are the growth rates linking to the power law (Garside, 1985), B&S (Burton et al., 1951) and BCF (Burton et al., 1951) models; S is supersaturation defined by the ratio between the solute concentration at a solution temperature and the solubility at the same temperature; S_{crit} is a critical value of supersaturation; k_G is the growth rate constant; r is the growth exponent; A_1 and A_2 are the thermodynamic parameters; ρ_s is the solute density; k_{MT} is the coefficient of mass transfer within the bulk of the solution; M_s is the solute molecular weight; C^* is the equilibrium concentration (solubility). The term $\frac{\rho_S}{k_{MT}\, C^* M_S}$ in Eqs. (S.1 – S.3) can be treated as a fitting parameter. In Eq. (S.1), if $r = 1$, it corresponds to a rough interface growth (RIG) mechanism (Weeks and Gilmer, 1979).

S3. MPB Solution Method

Whilst the theoretical solution of the MPB equation can only be obtained for some ideal (simple) cases, numerical solution methods can provide the most convenient and available approach. Lin et al. (Lin et al., 2016) developed an invariant method of moments to obtain analytical solution of a PB system, but this method could only be used for solving a one-dimensional homogeneous PB equation with size independent growth rate. Therefore, many other different numerical solution methods have been developed, for example, method of characteristics (Gunawan et al., 2004, Sotowa et al., 2000), moment of classes (David et al., 1995, Puel et al., 2003a), high resolution discretisation schemes (Gunawan et al., 2004, Ma et al., 2002, Wan et al., 2009), method of lines (Gerstlauer et al., 2001), finite-element schemes (Gerstlauer et al., 2006), moving grid techniques (Kumar and Ramkrishna, 1997), hierarchical solution strategies based on multilevel discretisation (Pinto et al., 2007, Sun and Immanuel, 2005), cell-ensemble method (Henson, 2005), Monte Carlo methods (Yu et al., 2015), etc. In this study, a discretisation method (moment of classes) has been used to solve the MPB equation (Eq. 1). In this, the three (x_1, x_2, x_3) size domains were discretised into i (i = 1, N_1), j (j = 1, N_2), k (k = 1, N_3) classes, respectively, where N_1, N_2, N_3 are the total number of classes for the (x_1, x_2, x_3) size domains and $\bar{x}_{1,i}(= x_{1,i} - x_{1,i-1}), \bar{x}_{2,j}(= x_{2,j} - x_{2,j-1}), \bar{x}_{3,k}(= x_{3,k} - x_{3,k-1})$ are the size of the i, j, k classes for the (x_1, x_2, x_3). Hence a group of $N_1 \times N_2 \times N_3$ ordinary differential equations below can be formulated and solved:

$$\begin{aligned}
&\frac{1}{V_T(t)}\frac{d}{dt}\left[V_T(t)\int_{x_{1,i-1}}^{x_{1,i}}\int_{x_{2,j-1}}^{x_{2,j}}\int_{x_{3,k-1}}^{x_{3,k}}\Phi(x_1,x_2,x_3,t)dx_1dx_2dx_3\right]+\\
&G_1(\bar{x}_{1,i},t)\left[\frac{x_{1,i+1}-x_{1,i}}{(x_{1,i}-x_{1,i-1})(x_{1,i+1}-x_{1,i-1})}\int_{x_{1,i-1}}^{x_{1,i}}\int_{x_{2,j-1}}^{x_{2,j}}\int_{x_{3,k-1}}^{x_{3,k}}\Phi(x_1,x_2,x_3,t)dx_1dx_2dx_3+\right.\\
&\left.\frac{x_{1,i}-x_{1,i-1}}{(x_{1,i+1}-x_{1,i})(x_{1,i+1}-x_{1,i-1})}\int_{x_{1,i}}^{x_{1,i+1}}\int_{x_{2,j-1}}^{x_{2,j}}\int_{x_{3,k-1}}^{x_{3,k}}\Phi(x_1,x_2,x_3,t)dx_1dx_2dx_3\right]+\\
&G_2(\bar{x}_{2,j},t)\left[\frac{x_{2,j+1}-x_{2,j}}{(x_{2,j}-x_{2,j-1})(x_{2,j+1}-x_{2,j-1})}\int_{x_{1,i-1}}^{x_{1,i}}\int_{x_{2,j-1}}^{x_{2,j}}\int_{x_{3,k-1}}^{x_{3,k}}\Phi(x_1,x_2,x_3,t)dx_1dx_2dx_3+\right.\\
&\left.\frac{x_{2,j}-x_{2,j-1}}{(x_{2,j+1}-x_{2,j})(x_{2,j+1}-x_{2,j-1})}\int_{x_{1,i-1}}^{x_{1,i}}\int_{x_{2,j}}^{x_{2,j+1}}\int_{x_{3,k-1}}^{x_{3,k}}\Phi(x_1,x_2,x_3,t)dx_1dx_2dx_3\right]+\\
&G_3(\bar{x}_{3,k},t)\left[\frac{x_{3,k+1}-x_{3,k}}{(x_{3,k}-x_{3,k-1})(x_{3,k+1}-x_{3,k-1})}\int_{x_{1,i-1}}^{x_{1,i}}\int_{x_{2,j-1}}^{x_{2,j}}\int_{x_{3,k-1}}^{x_{3,k}}\Phi(x_1,x_2,x_3,t)dx_1dx_2dx_3+\right.\\
&\left.\frac{x_{3,k}-x_{3,k-1}}{(x_{3,k+1}-x_{3,k})(x_{3,k+1}-x_{3,k-1})}\int_{x_{1,i-1}}^{x_{1,i}}\int_{x_{2,j-1}}^{x_{2,j}}\int_{x_{3,k}}^{x_{3,k+1}}\Phi(x_1,x_2,x_3,t)dx_1dx_2dx_3\right]=0 \qquad \text{(S.4)}
\end{aligned}$$

The $N_1 \times N_2 \times N_3$ ordinary differential equations obtained, together with initial and boundary conditions and also the equations for face-specific growth rates, and mass and heat balance in a batch cooling crystalliser, form a complete set of the PB solution system. Further detail can be found in literature (David et al., 1995, Ma et al., 2016, Ma and Wang, 2008, Ma et al., 2008, Puel et al., 2003a).

S4. Effect of Seeding Temperature

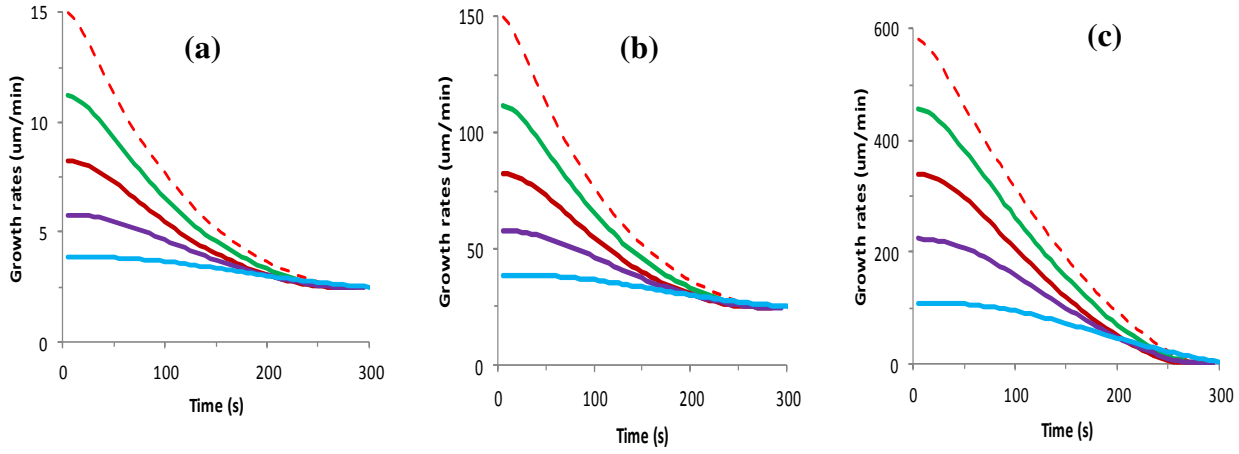

Figure S.1 Evolution of faceted growth rates during crystallisation processes in face direction of (a) face {101}, (b) face {10-1} and (c) face {011} under different seeding temperature (T_{seeds}) (or supersaturations (S_{seeds})) (T_{seeds} = 20.5°C (or S_{seeds} = 1.5) – dashed red line; T_{seeds} = 24.7°C (or S_{seeds} = 1.4) – green line; T_{seeds} = 28.9°C (or S_{seeds} = 1.3) – red line; T_{seeds} = 33.7°C (or S_{seeds} = 1.2) – blue line; T_{seeds} = 39.0°C (or S_{seeds} = 1.1) – light blue line).

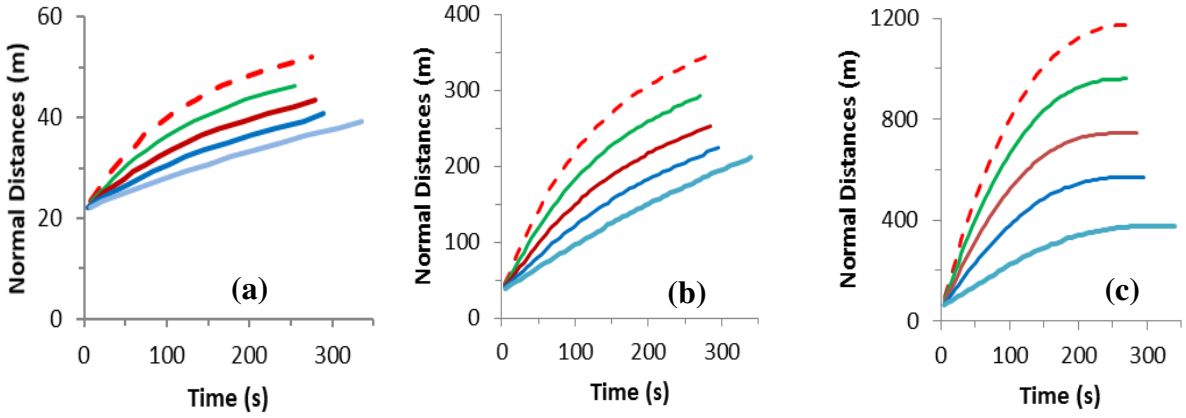

Figure S.2 Evolution of normal distances during crystallisation processes in face direction of (a) face {101}, (b) face {10-1} and (c) face {011} under different seeding temperature (T_{seeds}) (or supersaturations (S_{seeds})) (T_{seeds} = 20.5°C (or S_{seeds} = 1.5) – dashed red line; T_{seeds} = 24.7°C (or S_{seeds} = 1.4) – green line; T_{seeds} = 28.9°C (or S_{seeds} = 1.3) – red line; T_{seeds} = 33.7°C (or S_{seeds} = 1.2) – blue line; T_{seeds} = 39.0°C (or S_{seeds} = 1.1) – light blue line).

S5. Effect of Seed Loading

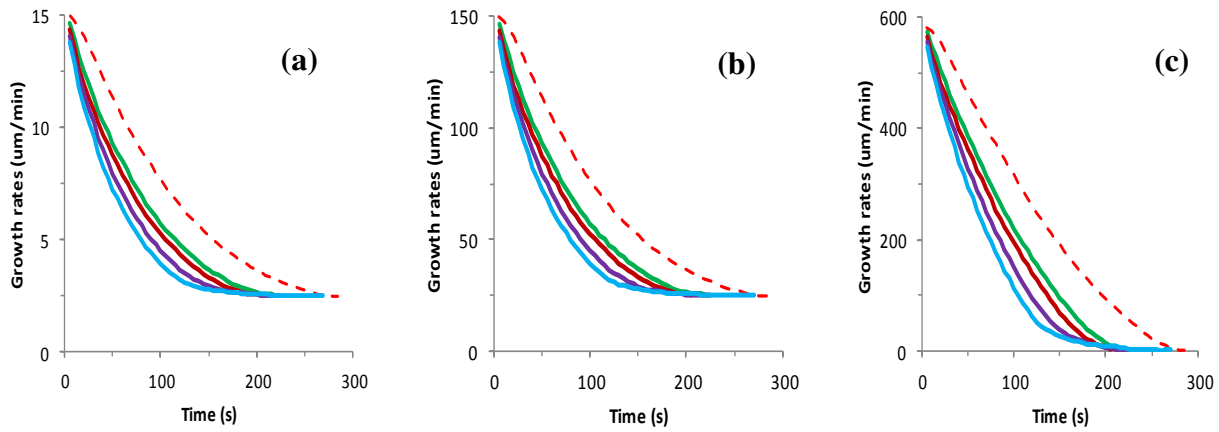

Figure S.3 Evolution of faceted growth rates during crystallisation processes in face direction of (a) face {101}, (b) face {10-1} and (c) face {011} under different seed loading (X_{seeds}) (X_{seeds} = 0.1% – dashed red line; X_{seeds} = 0.5% – green line; X_{seeds} = 1.0% – red line; X_{seeds} = 2.0% – purple line; X_{seeds} = 5.0% – blue line).

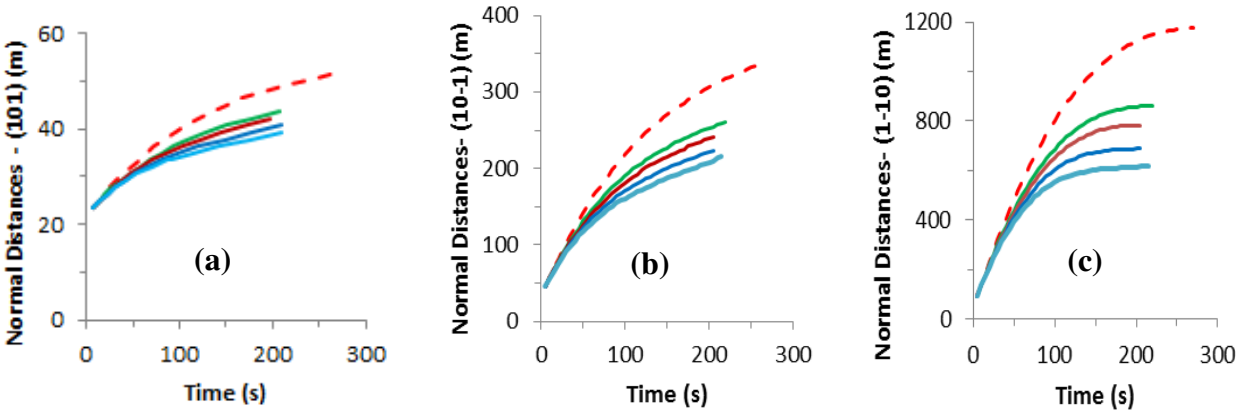

Figure S.4 Evolution of normal distances during crystallisation processes in face direction of (a) face {101}, (b) face {10-1} and (c) face {011} under different seed loading (X_{seeds}) (X_{seeds} = 0.1% – dashed red line; X_{seeds} = 0.5% – green line; X_{seeds} = 1.0% – red line; X_{seeds} = 2.0% – purple line; X_{seeds} = 5.0% – blue line).

S6. Effect of Seed Mean Shape

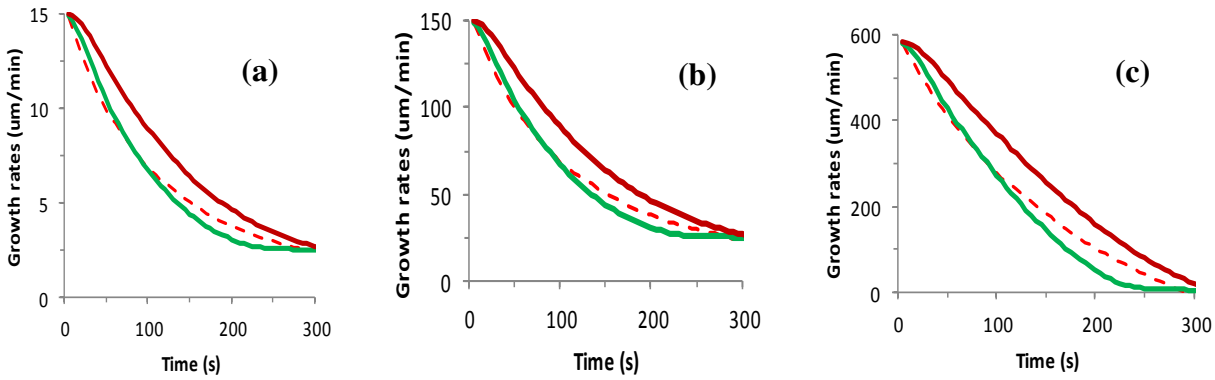

Figure S.5 Evolution of faceted growth rates during crystallisation processes in face direction of (a) face {101}, (b) face {10-1} and (c) face {011} under different seed mean shape (M_{seeds}) with standard deviations of σ_x, σ_y, σ_z = 8 μm (M_{seeds} = (22, 27, 6 μm) – dashed red line; M_{seeds} = (22, 27, 40 μm) – green line; M_{seeds} = (22, 27, 131 μm) – red line).

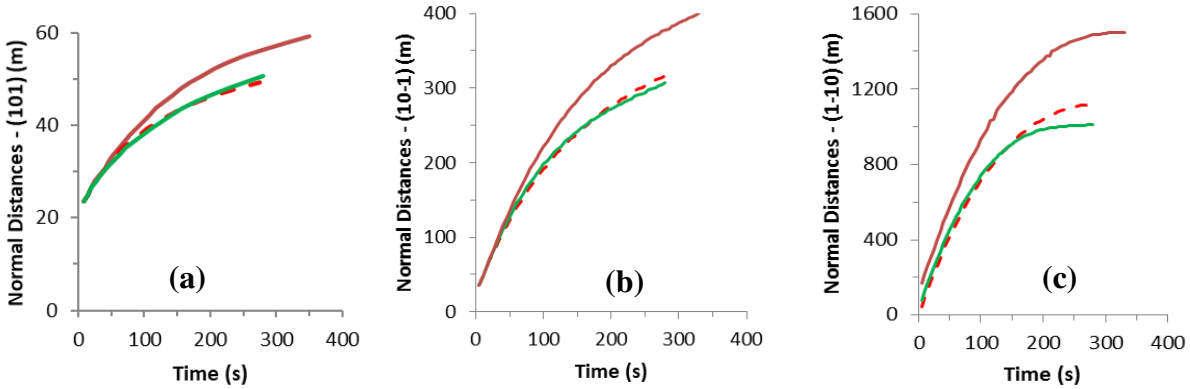

Figure S.6 Evolution of normal distances during crystallisation processes in face direction of (a) face {101}, (b) face {10-1} and (c) face {011} under different seed mean shape (M_{seeds}) with standard deviations of σ_x, σ_y, σ_z = 8 μm (M_{seeds} = (22, 27, 6 μm) – dashed red line; M_{seeds} = (22, 27, 40 μm) – green line; M_{seeds} = (22, 27, 131 μm) – red line).

S7. References

ALVAREZ, A. J. & MYERSON, A. S. 2010. Continuous plug flow crystallization of pharmaceutical compounds. *Crystal Growth & Design,* 10**,** 2219-2228.

BORCHERT, C., RAMKRISHNA, D., NERE, N., VOIGT, A. & SUNDMACHER, K. 2009. On the prediction of crystal shape distributions in a steady-state continuous crystallizer *Chemical Engineering Science,* 64**,** 686-696.

BORCHERT, C. & SUNDMACHER, K. 2012. Efficient formulation of crystal shape evolution equations. *Chemical Engineering Science,* 84**,** 85-99.
BRIESEN, H. 2009. Two-dimensional population balance modeling for shape dependent crystal attrition. *Chemical Engineering Science,* 64**,** 661-672.
BURTON, W. K., CABRERA, N. & FRANK, F. C. 1951. The growth of crystals and the equilibrium structure of their surfaces. *Philosophical Transactions of the Royal Society of London,* 243**,** 299-358.
CAILLET, A., SHEIBAT-OTHMAN, N. & FEVOTTE, G. 2007. Crystallization of monohydrate citric acid. 2. modeling through population balance equations. *Crystal Growth & Design,* 7**,** 2088-2095.
CAMACHO, D. M., ROBERTS, K. J., MULLER, F., THOMAS, D., MORE, I. & LEWTAS, K. 2017. Morphology and Growth of Methyl Stearate as a Function of Crystallization Environment. *Crystal Growth & Design,* 17**,** 563−575.
CHAKRABORTY, J., SINGH, M. R., RAMKRISHNA, D., BORCHERT, C. & SUNDMACHER, K. 2010. Modeling of crystal morphology distributions. Towards crystals with preferred asymmetry. *Chemical Engineering Science,* 65**,** 5676-5686.
DAVID, R., MARCHAL, P. & MARCANT, B. 1995. Modeling of Agglomeration in Industrial Crystallization from Solution. *Chemical Engineering & Technology,* 18**,** 302-309.
FEVOTTE, G., ALEXANDRE, C. & NIDA, S. O. 2007. A Population Balance Model of the solution-Mediated Phase Transition of citric acid. *AIChE Journal,* 53**,** 2578-2589.
GARSIDE, J. 1985. Industrial Crystallization from Solution. *Chemical Engineering Science,* 40**,** 3-26.
GERSTLAUER, A., GAHN, C., ZHOU, H., RAULS, M. & SCHREIBER, M. 2006. Application of population balances in the chemical industry - current status and future needs. *Chemical Engineering Science,* 61**,** 205-217.
GERSTLAUER, A., MITROVIC, A., MOTZ, S. & GILLES, E. D. 2001. A population model for crystallization processes using two independent particle properties. *Chemical Engineering Science,* 56**,** 2553-2565.
GUNAWAN, R., FUSMAN, I. & BRAATZ, R. D. 2004. High resolution algorithms for multidimensional population balance equations. *AIChE Journal,* 50**,** 2738-2749.
HENSON, M. A. 2005. Cell ensemble modeling of metabolic oscillations in continuous yeast cultures. *Computers & Chemical Engineering,* 29**,** 645-661.
HOUNSLOW, M. J., LEWIS, A. E., SANDERS, S. J. & BONDY, R. 2005. Generic crystallizer model: I. A model framework for a well-mixed compartment. *AIChE Journal,* 51**,** 2942-2955.
KUMAR, S. & RAMKRISHNA, D. 1997. On the solution of population balance equations by discretization — III. Nucleation, growth and aggregation of particles. *Chemical Engineering Science,* 52**,** 4659-4679.
KUVADIA, Z. B. & DOHERTY, M. F. 2013. Reformulating Multidimensional Population Balances for Predicting Crystal Size and Shape. *AIChE Journal,* 59**,** 3468-3474.
KWON, J. S., NAYHOUSE, M., CHRISTOFIDES, P. D. & ORKOULAS, G. 2013. Modeling and control of protein crystal shape and size in batch crystallization. *AIChE Journal,* 59**,** 2317-2327.
KWON, J. S., NAYHOUSE, M., CHRISTOFIDES, P. D. & ORKOULAS, G. 2014. Modeling and control of crystal shape in continuous protein crystallisation. *Chemical Engineering Science,* 107**,** 47-57.
LI, J., FREIREICH, B. J., WASSGREN, C. R. & LITSTER, J. D. 2013. Experimental validation of a 2-D population balance model for spray coating processes. *Chemical Engineering Science,* 95**,** 360-365.
LIN, F., FLOOD, A. E. & MELESHKO, S. V. 2016. Exact solutions of population balance equation. *Commun Nonlinear Sci Numer Simul,* 36**,** 378-390.

LIU, H. & LI, M. 2014. Two-compartmental population balance modeling of a pulsed spray fluidized bed granulation based on computational fluid dynamics (CFD) analysis. *International Journal of Pharmaceutics,* 475**,** 256-269.

LIU, J. J., HU, Y. D. & WANG, X. Z. 2013. Optimisation and control of crystal shape and size in protein crystallisation process. *Computers and Chemical Engineering,* 57**,** 133-140.

LIU, J. J., MA, C. Y., HU, Y. D. & WANG, X. Z. 2010a. Effect of seed loading and cooling rate on crystal size and shape distributions in protein crystallization—A study using morphological population balance simulation. *Computers and Chemical Engineering,* 34**,** 1945-1952.

LIU, J. J., MA, C. Y., HU, Y. D. & WANG, X. Z. 2010b. Modelling protein crystallisation using morphological population balance models. *Chemical Engineering Research & Design,* 88**,** 437-446.

LOVETTE, M. A., BROWNING, A. R., GRIFFIN, D. W., SIZEMORE, J. P., SNYDER, R. C. & DOHERTY, M. F. 2008. Crystal Shape Engineering. *Industrial & Engineering Chemistry Research,* 47**,** 9812-9833.

MA, C. Y., LIU, J. J. & WANG, X. Z. 2016. Measurement, modelling, and closed-loop control of crystal shape distribution: Literature review and future perspectives. *Particuology,* 26**,** 1-18.

MA, C. Y. & ROBERTS, K. J. 2018. Combining Morphological Population Balances with Face-Specific Growth Kinetics Data to Model and Predict the Crystallization Processes for Ibuprofen. *Ind Chem Eng Res,* 57**,** 16379-16394.

MA, C. Y. & WANG, X. Z. 2008. Crystal growth rate dispersion modelling using morphological population balance. *AIChE Journal,* 54**,** 2321-2334.

MA, C. Y. & WANG, X. Z. 2012. Model identification of crystal facet growth kinetics in morphological population balance modeling of L-glutamic acid crystallization and experimental validation. *Chemical Engineering Science,* 70**,** 22-30.

MA, C. Y., WANG, X. Z. & ROBERTS, K. J. 2007. Multi-dimensional population balance modelling of the growth of rod-like L-glutamic acid crystals using growth rates estimated from in-process imaging. *Advanced Powder Technology,* 18**,** 707-723.

MA, C. Y., WANG, X. Z. & ROBERTS, K. J. 2008. Morphological population balance for modelling crystal growth in individual face directions. *AIChE Journal,* 54**,** 209-222.

MA, D. L., TAFTI, D. K. & BRAATZ, R. D. 2002. High-resolution simulation of multidimensional crystal growth. *Industrial & Engineering Chemistry Research,* 41**,** 6217-6223.

MAJUMDER, A. & NAGY, Z. K. 2013. Prediction and control of crystal shape distribution in the presence of crystal growth modifiers *Chemical Engineering Science,* 101 593-602.

MARCHAL, P., DAVID, R., KLEIN, J. P. & VILLERMAUX, J. 1988. Crystallization and precipitation engineering .1. An efficient method for solving population balance in crystallization with agglomeration. *Chemical Engineering Science,* 43**,** 59-67.

MENON, A. R., KRAMER, H. J. M., GRIEVINK, J. & JANSENS, P. J. 2005. Modelling the cyclic behaviour in a DTB crystallizer - a two-population blance model approach. *Journal of Crystal Growth,* 275**,** e1373-e1381.

MERSMANN, A., BRAUN, B. & LOFFELMANN, M. 2002. Prediction of crystallisation coefficients of the population balance. *Chemical Engineering Science,* 57**,** 4267-4275.

MULLIN, J. W. 2001. *Crystallization,* USA, Butterworth-Heinemann.

OULLION, M., PUEL, F., FEVOTTE, G., RIGHINI, S. & CARVIN, P. 2007. Industrial batch crystallization of a plate-like organic product. In situ monitoring and 2D-CSD modelling: Part 1: Experimental study. *Chemical Engineering Science,* 62**,** 820-832.

PATIENCE, D. B., DELL'ORCO, P. C. & RAWLINGS, J. B. 2004. Optimal Operation of a Seeded Pharmaceutical Crystallization with Growth-Dependent Dispersion. *Organic Process Research & Development,* 8**,** 609-615.

PINTO, M. A., IMMANUEL, C. D. & DOYLE, F. J. 2007. A feasible solution technique for higher-dimensional population balance models. *Computers & Chemical Engineering,* 31**,** 1242-1256.

PUEL, F., FEVOTTE, G. & KLEIN, J. P. 2003a. Simulation and analysis of industrial crystallization processes through multidimensional population balance equations. Part 1: a resolution algorithm based on the method of classes. *Chemical Engineering Science,* 58**,** 3715-3727.

PUEL, F., FEVOTTE, G. & KLEIN, J. P. 2003b. Simulation and analysis of industrial crystallization processes through multidimensional population balance equations. Part 2: a study of semi-batch crystallization. *Chemical Engineering Science,* 58**,** 3729-3740.

RAMKRISHNA, D. & MAHONEY, A. W. 2002. Population balance modeling. Promise for the future. *Chemical Engineering Science,* 57**,** 595-606.

RAWLINGS, J. B., WITKOWSKI, W. R. & EATON, J. W. 1992. Modelling and control of crystallizers. *Powder Technology,* 69**,** 3-9.

SATO, K., NAGAI, H., HASEGAWA, K., TOMORI, K., KRAMER, H. J. M. & JANSENS, P. J. 2008. Two-dimensional population balance model with breakage of high aspect ratio crystals for batch crystallization. *Chemical Engineering Science,* 63**,** 3271-3278.

SHI, D., EL-FARRA, N. H., LI, M., MHASKAR, P. & CHRISTOFIDES, P. D. 2006. Predictive control of particle size distribution in particulate processes. *Chemical Engineering Science,* 61**,** 268-281.

SOTOWA, K. I., NAITO, K., KANO, M., HASEBE, S. & HASHIMOTO, I. 2000. Application of the method of characteristics to crystallizer simulation and comparison with finite difference for controller performance evaluation. *Journal of Process Control,* 10**,** 203-208.

SUN, N. F. & IMMANUEL, C. D. 2005. Efficient solution of population balance models employing a hierarchical solution strategy based on a multi-level discretization. *Transactions of the Institute of Measurement and Control,* 27**,** 347-366.

TEMMEL, E., EISENSCHMIDT, H., LORENZ, H., SUNDMACHER, K. & SEIDEL-MORGENSTERN, A. 2016. A Short-Cut Method for the Quantification of Crystallization Kinetics. 1. Method Development. *Crystal Growth & Design,* 16**,** 6743-6755.

ULBERT, Z. & LAKATOS, B. G. 2005. Modelling and simulation of crystallisers under non-perfect micromixing conditions. *Chemical Engineering Science,* 60**,** 3525-3536.

VETTER, T., BURCHAM, C. L. & DOHERTY, M. F. 2014. Regions of attainable particle sizes in continuous and batch crystallisation processes. *Chemical Engineering Science,* 106**,** 167-180.

WAN, J., WANG, X. Z. & MA, C. Y. 2009. Particle shape manipulation and optimization in cooling crystallization involving multiple crystal morphological forms. *AIChE Journal,* 55**,** 2049-2061.

WANG, X. Z. & MA, C. Y. 2009. Morphological population balance model in principal component space. *AIChE Journal,* 55**,** 2370-2381.

WANG, X. Z., ROBERTS, K. J. & MA, C. Y. 2008. Crystal growth measurement using 2D and 3D imaging and the perspectives for shape control. *Chemical Engineering Science,* 63**,** 1171-1184.

WARD, J. D., MELLICHAMP, D. A. & DOHERTY, M. F. 2006. Choosing an operating policy for seeded batch crystallization. *AIChE Journal,* 52**,** 2046-2054.

WARD, J. D., YU, C.-C. & DOHERTY, M. F. 2011. A New Frameowrk and a Simpler Method for the Development of Batch Crytsallisation Recipes. *AIChE Journal,* 57**,** 606-617.

WEEKS, J. D. & GILMER, G. H. 1979. Dynamics of crystal growth. *Advances in Chemical Physics,* 40**,** 157-227.

YU, X., HOUNSLOW, M. J. & REYNOLDS, G. K. 2015. Monte Carlo solution of population balance equations. *AIChE Journal,* 61**,** 2394-2402.

ZHANG, Y. C. & DOHERTY, M. F. 2004. Simultaneous prediction of crystal shape and size for solution crystallization. *AIChE Journal,* 50**,** 2101-2112.